Supplementary Information

Rationally Designed Tetrahedral-Configuration-Matching Methane Trap in a Metal–Organic Framework for Efficient CH_4/N_2 Separation

Yating Wang,[a] Feifei Zhang,[a] Yanan Yang,[a] Xiaoqing Wang,[a] Jinping Li *[ab] and Jiangfeng Yang *[a]*

[a] College of Chemistry and Chemical Engineering, Taiyuan University of Technology, Taiyuan 030024, Shanxi Province, China

[b] Shanxi Research Institute of Huairou Laboratory, Taiyuan 030031, Shanxi Province, China

*Corresponding author:

E-mail: zhangfeifei0096@link.tyut.edu.cn;

E-mail: jpli211@hotmail.com;

E-mail: yangjiangfeng@tyut.edu.cn

Table of Contents

Experimental Procedures

Chemicals

Nickel(II) chloride hexahydrate ($NiCl_2 \cdot 6H_2O$, 98%) was purchased from Aladdin. Norfloxacin ($C_{16}H_{18}FN_3O_3$, 98%), ciprofloxacin ($C_{17}H_{18}FN_3O_3$, 98%), and 4-tert-butylsulfonylcalix[4]arene ($C_{44}H_{56}O_6S_4$, 98%) were obtained from Innochem and TCI, respectively. Methanol (CH_3OH) and N,N-dimethylformamide (DMF, C_3H_7NO) were provided by Sinopharm Chemical Reagent Co., Ltd. All reagents were used as received without further purification. Deionized water used in the experiments was prepared in our laboratory.

Synthesis of TUTJ-2Ni and TUTJ-3Ni

$NiCl_2 \cdot 6H_2O$ (59.4 mg, 0.25 mmol), ciprofloxacin (24.8 mg, 0.15 mmol), and $H_4SC4A\text{-}SO_2$ (42.4 mg, 0.05 mmol) were dissolved in a mixed solvent of methanol (3 mL) and DMF (5 mL) in a 20 mL scintillation vial. The mixture was sonicated for 0.5 h to afford a homogeneous solution. The vial was then heated at 373 K for 24 h. After cooling slowly to room temperature, the resulting crystalline product was collected by filtration, washed three times with methanol, and dried under ambient conditions to give TUTJ-3Ni as a green solid (yield: approximately 70 mg). The conversion rates of the precursors are calculated as 88.8% for ciprofloxacin, 66.6% for $H_4SC4A\text{-}SO_2$, and 53.3% for $NiCl_2 \cdot 6H_2O$, achieving a final yield of 88.8%. TUTJ-2Ni was obtained under identical reaction conditions by replacing ciprofloxacin with norfloxacin (23.9 mg, 0.15 mmol).

Scalable synthesis of TUTJ-3Ni

TUTJ-3Ni was synthesized on an enlarged scale under solvothermal conditions. The detailed procedure is as follows: $NiCl_2 \cdot 6H_2O$ (5.94 g, 20.5 mmol), ciprofloxacin (2.48 g, 7.5 mmol), and $H_4SC4A\text{-}SO_2$ (4.24 g, 5.0 mmol) were dissolved in a mixed solvent of methanol (150 mL) and dimethylformamide (250 mL) in a 500 mL vial. The mixture was stirred at room temperature for 1 hour to ensure complete dissolution. The reaction system was then heated statically at 373 K for 72 hours. After slowly cooling to room temperature, thoroughly washed with methanol (3×50 mL) and dried at room temperature, affording TUTJ-3Ni as a green crystalline solid (yield: approximately 8.6 g).

Characterization

Powder X-ray diffraction (PXRD) patterns were recorded on a Bruker D8 Advance diffractometer using Cu Kα radiation (λ = 1.5418 Å), with the 2θ range set from 5° to 30° at a scanning rate of 5° min^{-1}. The operating voltage and current were 40 kV and 40 mA, respectively. Scanning electron microscopy (SEM) images were acquired using a Zeiss Sigma 300 microscope at an accelerating voltage of 5 kV. Energy-dispersive X-ray spectroscopy (EDS) was carried out on a Smart EDX system equipped with X-ray mapping at an accelerating voltage of 15 kV. Thermogravimetric analysis (TGA) was performed on a Netzsch STA 449 F5 thermal analyzer under an air atmosphere, with a heating rate of 10 K min^{-1} from 303 K to 1073 K. Nitrogen adsorption–desorption isotherms at 77 K were measured using a Micromeritics 3Flex analyzer. Prior to measurement, the samples were activated at 423 K under high vacuum (1×10^{-5} mbar) for 8 h. The Brunauer–Emmett–Teller (BET) method was applied to calculate the specific surface area. Pore size distributions and logarithmic pore volume plots for TUTJ-2Ni and TUTJ-3Ni were derived using non-local density functional theory (NLDFT) based on the N_2 adsorption data. Fourier-transform infrared (FTIR) spectra were recorded on a Shimadzu IRTracer-100 spectrometer using KBr pellets. The samples were thoroughly dried at 423 K for 2 h prior to measurement, and spectra were collected in the range of 4000-700 cm^{-1}. CH_4 and N_2 single-component gas adsorption isotherms were measured using an APSP 2460 analyzer. Prior to measurements, the TUTJ-3Ni sample (approximately 100 mg) was degassed at 423 K under high vacuum (1×10^{-5} mbar) for 8 h, during which the sample color changed from green to yellow. For CH_4 adsorption-desorption cycling tests, the desorption process was achieved by gradually reducing the pressure to high vacuum (1×10^{-5} mbar) at 298 K, followed immediately by the next adsorption measurement. This sequence was repeated for multiple cycles to evaluate the regeneration performance. Kinetic adsorption studies were conducted using an Intelligent Gravimetric Analyzer (IGA-001, Hiden Isochema), with samples similarly degassed at 423 K prior to analysis.

Fitting of pure component isotherms

Following activation at 423 K under high vacuum (1×10^{-5} mbar) for 8 h, the single-component adsorption isotherms of CH_4 and N_2 were measured using an ASAP-2460 analyzer at 298 K. The obtained isotherms were fitted using the dual-site Langmuir-Freundlich (DSLF) model, which effectively describes adsorption on heterogeneous surfaces featuring two distinct types of adsorption sites. The DSLF equation is expressed as:

$$q = q_1 \frac{b_1 p^{1/n_1}}{1 + b_1 p^{1/n_1}} + q_2 \frac{b_2 p^{1/n_2}}{1 + b_2 p^{1/n_2}}. \qquad \text{* MERGEFORMAT (1)}$$

Where q represents the equilibrium adsorption capacity ($cm^3\ g^{-1}$), q_1 and q_2 denote the saturation uptake capacities ($cm^3\ g^{-1}$) for site types 1 and 2, respectively, b_1 and b_2 are the affinity coefficients (bar^{-1}) of the two sites, and n_1 and n_2 describe the deviations from ideal surface homogeneity. The DSLF model exhibited excellent agreement with the experimental data, yielding correlation coefficients (R^2) greater than 0.999 for both CH_4 and N_2 isotherms.

Isosteric heat of adsorption

The isosteric heats of adsorption (Q_{st}) of CH_4 and N_2 on TUTJ materials were calculated from single-component adsorption isotherms measured at 273 K, 298 K, and 313 K using the Clausius-Clapeyron equation. This approach allows for the quantification of adsorption energetics and surface heterogeneity based on temperature-dependent adsorption behavior.

The Clausius-Clapeyron equation is expressed as:

$$Q_{st} = R \cdot \frac{T_1 T_2}{T_2 - T_1} \cdot \ln\left(\frac{P_2}{P_1}\right) \qquad \text{* MERGEFORMAT (2)}$$

Where Q_{st} represents the isosteric heat of adsorption (kJ mol^{-1}), R is the universal gas constant (8.314 J mol^{-1} K^{-1}), T_1 and T_2 are the measurement temperatures (K), and P_1 and P_2 are the pressures (bar) corresponding to the same adsorbed amount on the adsorption isotherms at temperatures T_1 and T_2, respectively.

Ideal Adsorbed Solution Theory (IAST) Calculations

IAST was employed to predict the adsorption behavior of gas mixtures in TUTJ materials, based on the measured single-component isotherms. This theoretical framework assumes ideal mixing of adsorbates in the adsorbed phase and enables the calculation of mixture equilibria from pure component data. The selectivity of component 1 over component 2 in a binary mixture is defined as:

$$S_{ads} = \frac{q_1 / q_2}{p_1 / p_2} \qquad \text{* MERGEFORMAT (3)}$$

Where q_1 and q_2 represent the equilibrium adsorption capacities (cm^3 g^{-1}) of components 1 and 2 in the adsorbed phase, and P_1 and P_2 denote their respective partial pressures (bar) in the bulk gas phase.

Diffusional time constants and kinetic selectivity

The diffusional time constants (D and D/r^2) were determined using the short-time approximation of the Fickian diffusion model, based on the following assumptions: a step change in gas-phase concentration, initially clean adsorbent beds, and micropore diffusion as the rate-controlling mechanism. The governing equation is expressed as:

$$\frac{q_t}{q_\infty} = \frac{6}{\sqrt{\pi}} \sqrt{\frac{Dt}{r^2}} \qquad \text{* MERGEFORMAT (4)}$$

Where q_t represents the gas uptake at time t, q_∞ denotes the equilibrium gas uptake, D is the intracrystalline diffusivity, and r is the radius of the equivalent spherical particle. The time constants were obtained from the slopes of the linear regions in the $\frac{q_t}{q_\infty}$ versus $\sqrt{t}$ plots at low gas uptake ranges.

The kinetic selectivity for CH_4/N_2 was calculated using the following relationship:

$$K_{ij} = \frac{D_i'}{D_j'} \qquad \text{¥* MERGEFORMAT (5)}$$

Where D_i' and D_j' present the diffusional time constants for methane and nitrogen, respectively.

In-situ IR spectroscopic analysis

In situ IR spectra of adsorbed CH_4 and N_2 were collected at room temperature using a Bruker V70 spectrometer equipped with an MCT detector and a stainless steel in situ IR cell with KBr windows. The spectral resolution was set to 4 cm^{-1}. Prior to measurement, the adsorbent powder was evenly placed in the sample cup of the reaction cell. The TUTJ samples were activated at 423 K under high vacuum (1×10^{-5} mbar) for 8 h. During activation, the heating and cooling rates were maintained at 5 K min^{-1}. After cooling to room temperature, the background spectrum of the activated sample was immediately recorded. Subsequently, CH_4 and N_2 adsorption measurements were performed sequentially until saturation was reached.

Theoretical calculation methods

All calculations and simulations in this study were performed using BIOVIA Materials Studio. Grand Canonical Monte Carlo (GCMC) simulations in the adsorption module were employed to investigate the adsorption behavior of CH_4 and N_2 in TUTJ-2Ni and TUTJ-3Ni at 298 K over the pressure range of 0.1-1.0 bar. For each state point, the Metropolis algorithm was implemented with an equilibrium stage of 1.0×10^7 steps. The framework atoms were fixed at their crystallographic positions, treating the materials as rigid structures, with interatomic interactions described by the COMPASSIII force field [1-3]. Van der Waals interactions were computed using the Lennard-Jones potential with a cutoff radius of 18.5 Å. Long-range electrostatic interactions were evaluated using the Ewald summation method with an accuracy of 1.0×10^{-5} kcal mol^{-1}. The crystal structures of TUTJ-2Ni and TUTJ-3Ni and gas molecules were optimized using dispersion-corrected density functional theory (DFT-D),

followed by single-point energy calculations. Geometry optimization was carried out on the CASTEP platform employing the Perdew-Burke-Ernzerhof (PBE) exchange-correlation functional within the generalized gradient approximation (GGA)[4]. Convergence criteria included atomic forces below 0.03 eV Å^{-1} and energy convergence of 1.0×10^{-5} eV atom^{-1}.

The binding energy (E_b) for the adsorption process was calculated using the following equation:

$$E_b = E_{\mathrm{MOF}} + E_{\mathrm{gas}} - E_{\mathrm{gas+MOF}} \qquad \text{* MERGEFORMAT (6)}$$

Where E_{MOF} represents the energy of the optimized bare MOF framework, E_{gas} denotes the energy of the isolated gas molecule, and $E_{\mathrm{gas+MOF}}$ corresponds to the energy of the optimized gas-MOF complex. More negative binding energies indicate stronger interactions between the adsorbate molecules and the framework.

Geometry optimizations were conducted using the B3LYP-D3(BJ)/6-31G(d) basis set with Gaussian 09 package[5]. IGMH analysis were conducted to visualize the intermolecular interactions using Multiwfn 3.8[6] and were rendered with VMD 1.9.3 software[7].

Breakthrough experiment

The breakthrough experimental system employed in this study comprises three integrated components: a gas delivery unit with mass flow controllers, a fixed-bed adsorption column, and a mass spectrometer (HPR-20 EGA, Hiden Analytical, UK) for real-time effluent analysis. Breakthrough curves for TUTJ-3Ni were systematically measured at 298 K using CH_4/N_2 mixtures with varying compositions at total flow rates ranging from 5 to 20 mL min^{-1}. For performance benchmarking, parallel breakthrough experiments were conducted under identical conditions using TUTJ-2Ni, ATC-Cu, Ni(ina)$_2$, and CoNi-TED adsorbents.

All adsorbents, including TUTJ-3Ni (0.93 g), TUTJ-2Ni (0.73 g), ATC-Cu (1.03 g), Ni(ina)$_2$ (0.87 g), and CoNi-TED (0.64 g), were activated following a standardized protocol: heating at 433 K under high vacuum (1×10^{-5} mbar) for 12 hours. The activated materials were then packed into adsorption columns (Φ 4.0 × 100 mm) under controlled anhydrous conditions. Prior to each measurement, the adsorption column was purged with helium (99.999% purity) at 10 mL min^{-1} for 30 minutes to establish baseline conditions. The feed was subsequently switched to the target CH_4/N_2 mixture at the specified flow rate while maintaining system temperature at 298 K and ordinary pressure. Between consecutive tests, the adsorbent bed was regenerated by helium purging (10 mL min^{-1}) for 20 minutes at ambient temperature. For breakthrough tests under humid conditions, a 100% RH environment was simulated using pure water vapor. A CH_4/N_2 mixed feed gas was passed through the adsorption bed at a flow rate of 5 mL min^{-1}, and the outlet gas composition was analyzed using a mass spectrometer.

The kinetic adsorption capacity and breakthrough selectivity

The kinetic adsorption capacity (Q) of CH_4 or N_2 was calculated using the following equation:

$$Q = \frac{\upsilon \times y}{22.4} \times \int_{t_1}^{t_2} (c_0 - c_t)dt = \frac{\upsilon \times y}{22.4} \times S \qquad \text{* MERGEFORMAT (7)}$$

Where υ represents the flow rate of the gas mixture (mL min^{-1}), y is the molar fraction of CH_4 or N_2 in the feed gas, and S denotes the integrated area between the concentration-time curve and the baseline. Specifically, the integrated area for N_2 corresponds to S_1-S_3, while for CH_4 it is S_1+S_2.

Based on the dynamic adsorption capacities of the components, the dynamic separation selectivity was calculated as:

$$S_{CH_4/N_2} = \frac{Q_{CH_4} / Q_{N_2}}{y_{CH_4} / y_{N_2}} \qquad \text{* MERGEFORMAT (8)}$$

Supporting Table and Figures

Table S1 Comparison of molecular sizes and physical properties of CH_4 and N_2.

Compounds	Boiling point (K)	Kinetic diameter(nm)	Polarizability ($x10^{-25}cm^3$)	Dipole moment ($x10^{18}$esu cm)	Quadrupole moment ($x10^{26}$esu cm)
CH_4	**111.66**	**0.38**	**25.93**	**0**	**0**
N_2	77.35	0.36	17.40	**0**	**1.52**

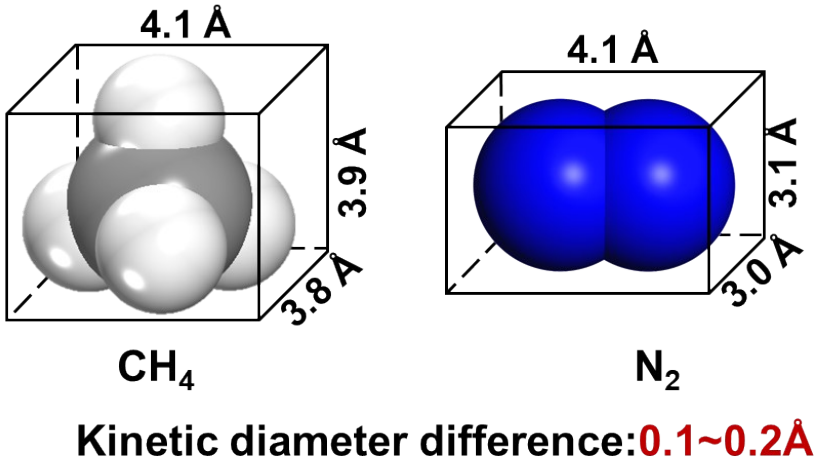

Figure S1. Molecular dimension of CH_4 and N_2.

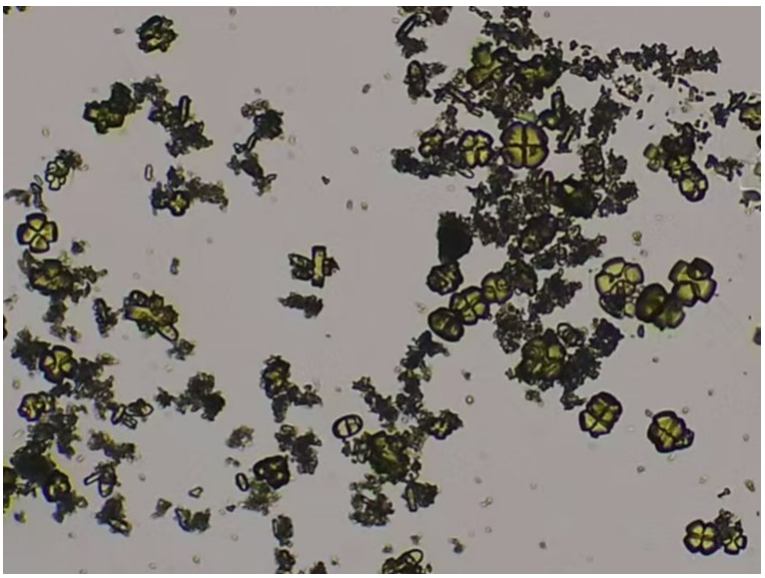

Figure S2. Single crystal photograph of TUTJ-3Co.

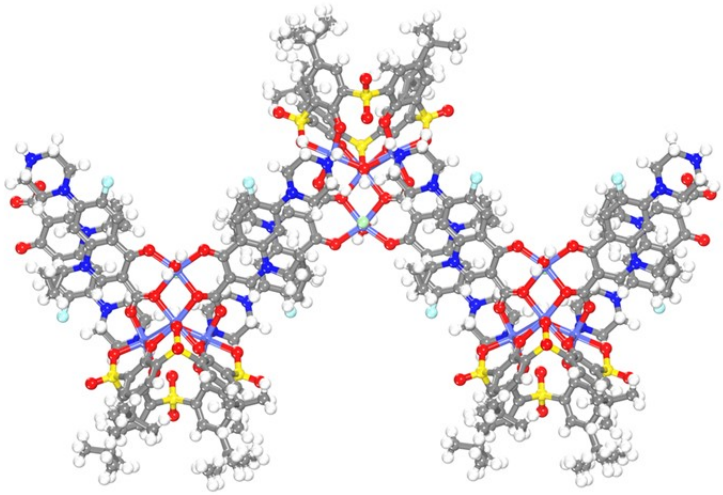

Figure S3. The single crystal structure of TUTJ-3Co.

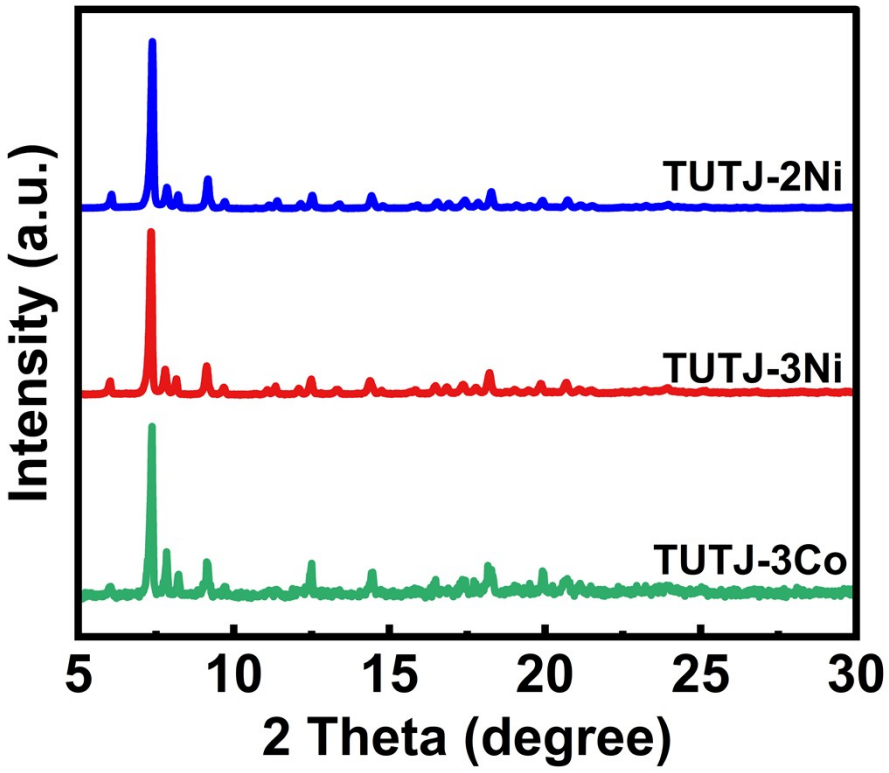

Figure S4. XRD patterns of TUTJ-2Ni, TUTJ-3Ni, and TUTJ-3Co.

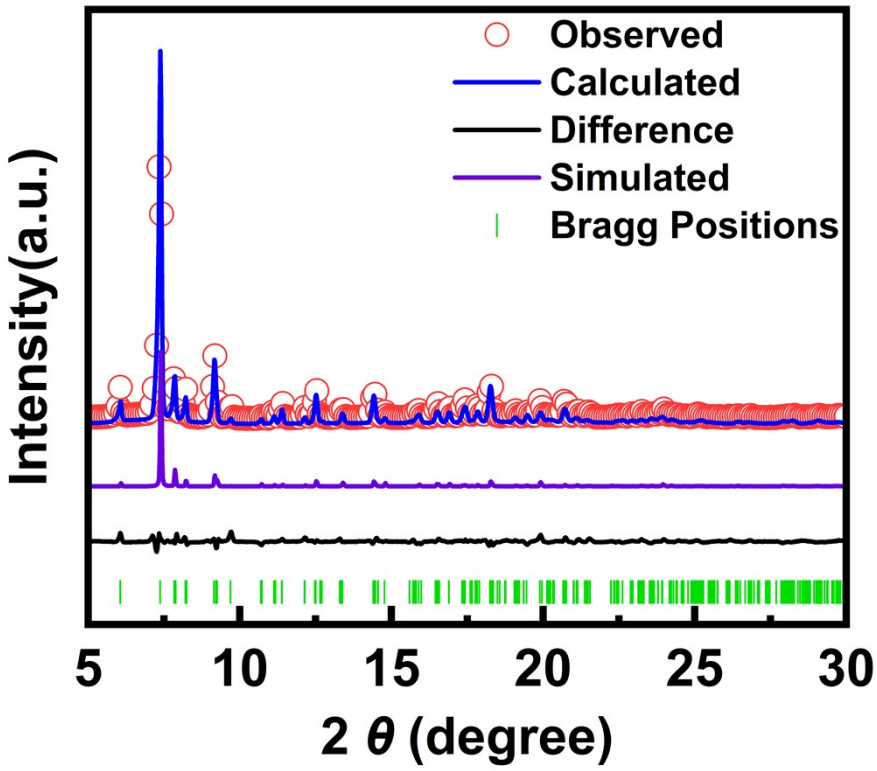

Figure S5. Rietveld refinement of TUTJ-2Ni. The experimental powder X-ray diffraction pattern is depicted in red, while the refined pattern appears in blue. The discrepancy between the observed and refined profiles is illustrated in gray, the standard reference pattern is shown in purple, and the Bragg positions derived from the crystal structure are indicated in green.

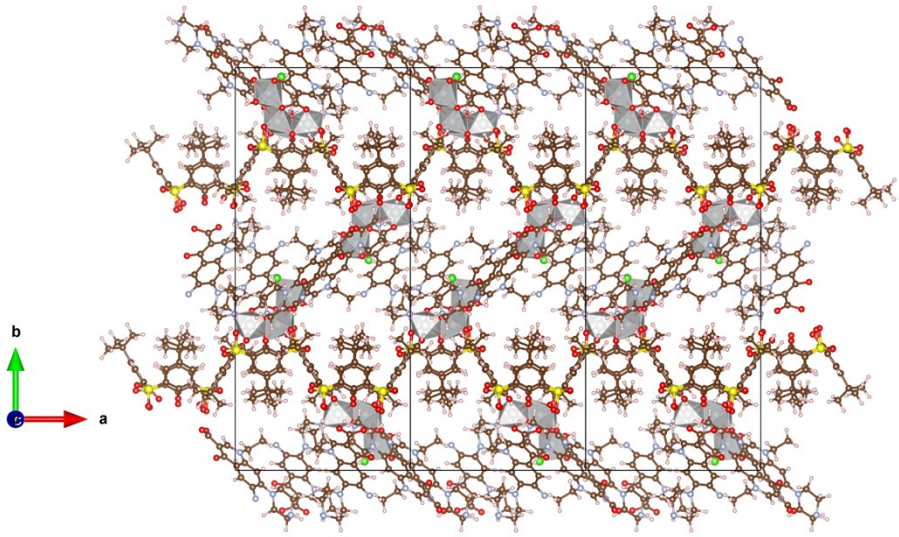

Figure S6. The crystal structure of TUTJ-2Ni.

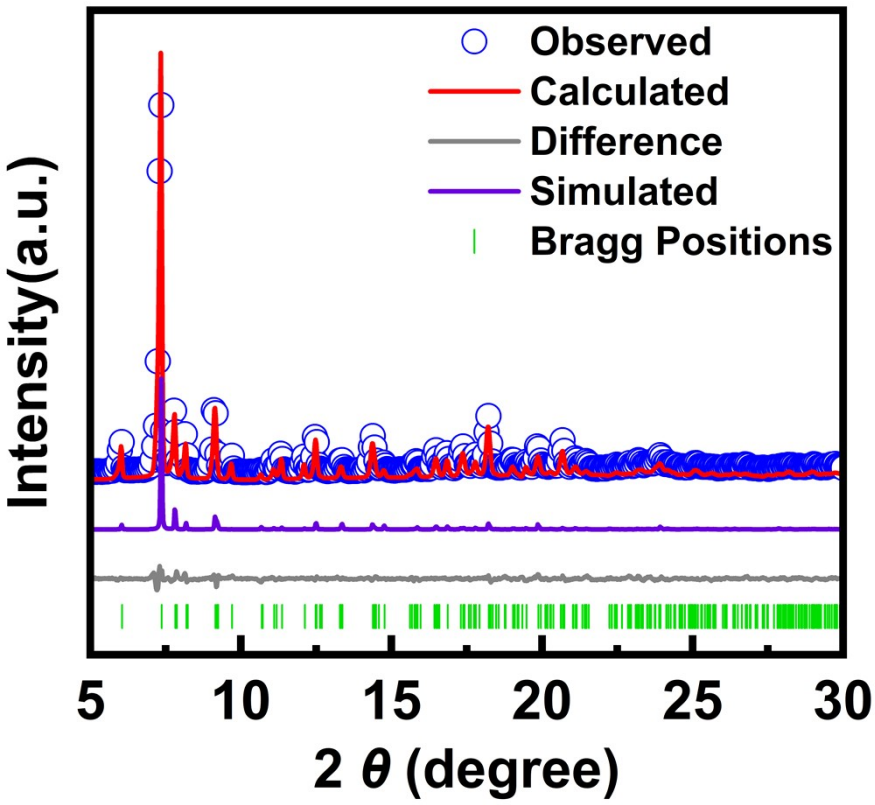

Figure S7. Rietveld refinement of TUTJ-3Ni. The experimental powder X-ray diffraction pattern is depicted in blue, while the refined pattern appears in red. The discrepancy between the observed and refined profiles is illustrated in gray, the standard reference pattern is shown in purple, and the Bragg positions derived from the crystal structure are indicated in green.

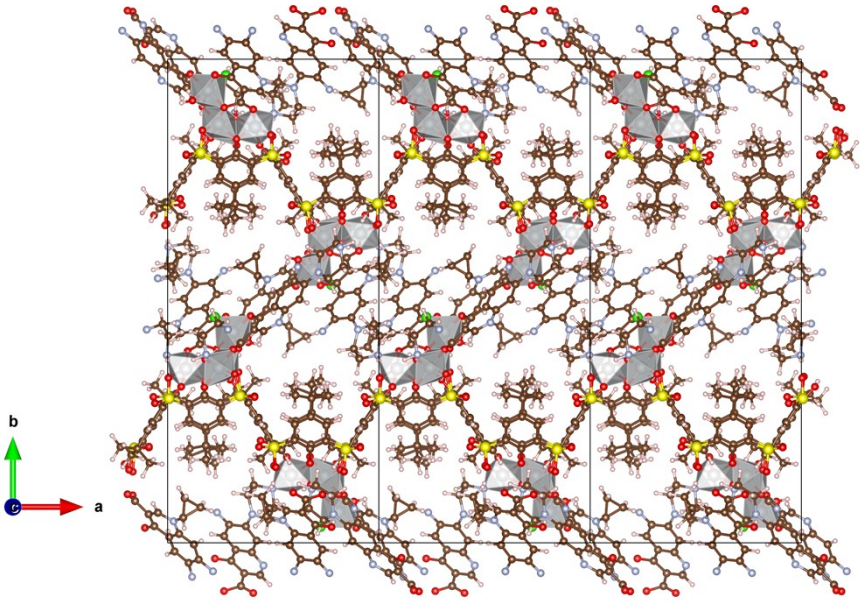

Figure S8. The crystal structure of TUTJ-3Ni.

Table S2 Crystallographic data of TUTJ-2Ni and TUTJ-3Ni.

Compound	**TUTJ-2Ni**	**TUTJ-3Ni**
CCDC	2492179	2492185
sp. gr.	P 21/n	P 21/n
a (Å)	15.8926	15.9194
b (Å)	36.4744	36.4118
c (Å)	15.8970	15.9193
α (°)	90.0000	90.0000
β (°)	90.3155	90.3552
γ (°)	90.0000	90.0000
V ($Å^3$)	9214.88	9227.52
2θ-interval	5°-120°	5°-120°
no. of reflection	13814	13818
R_{wp} (%)	5.79	5.24
R_p (%)	3.82	3.28
R_{exp} (%)	3.58	4.38
χ^2	1.62	1.20

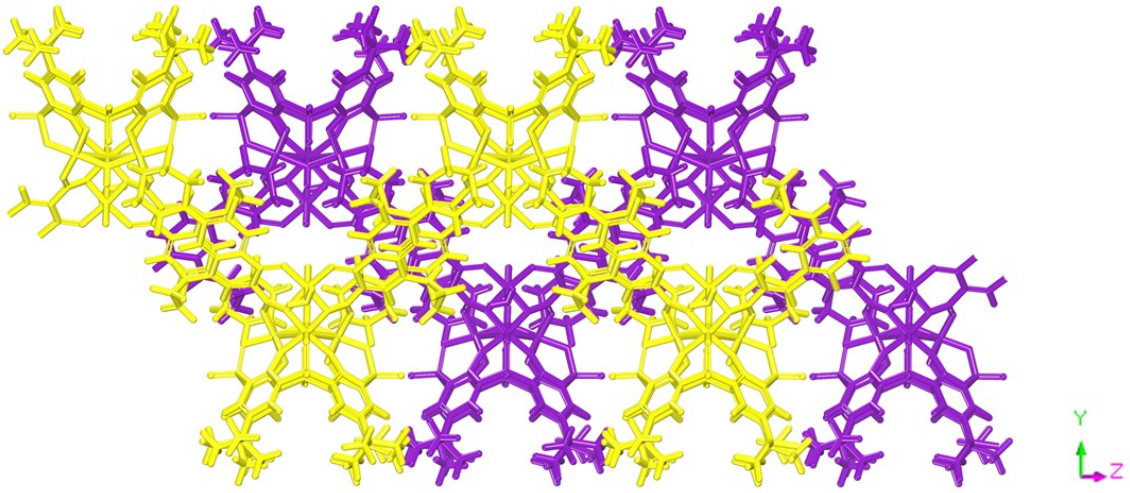

Figure S9. Chain-like arrangement structure of TUTJ-3Ni.

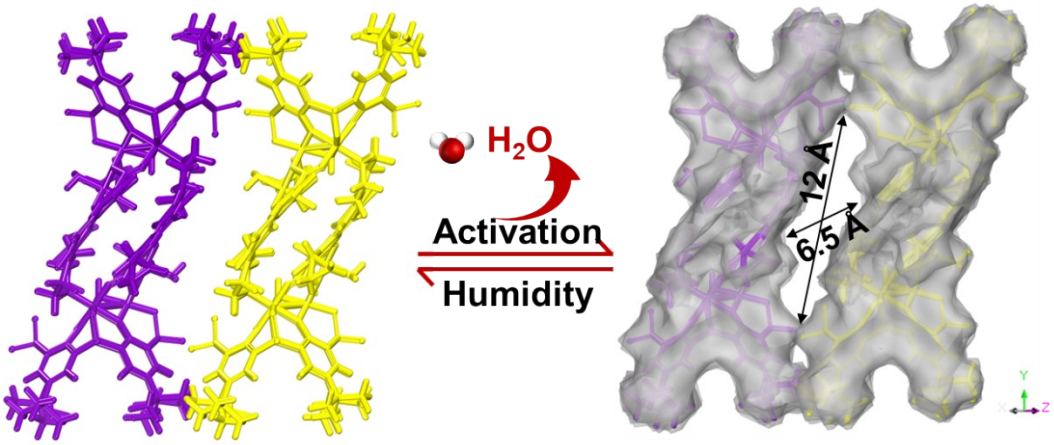

Figure S10. Evolution of porosity in TUTJ-3Ni during activation.

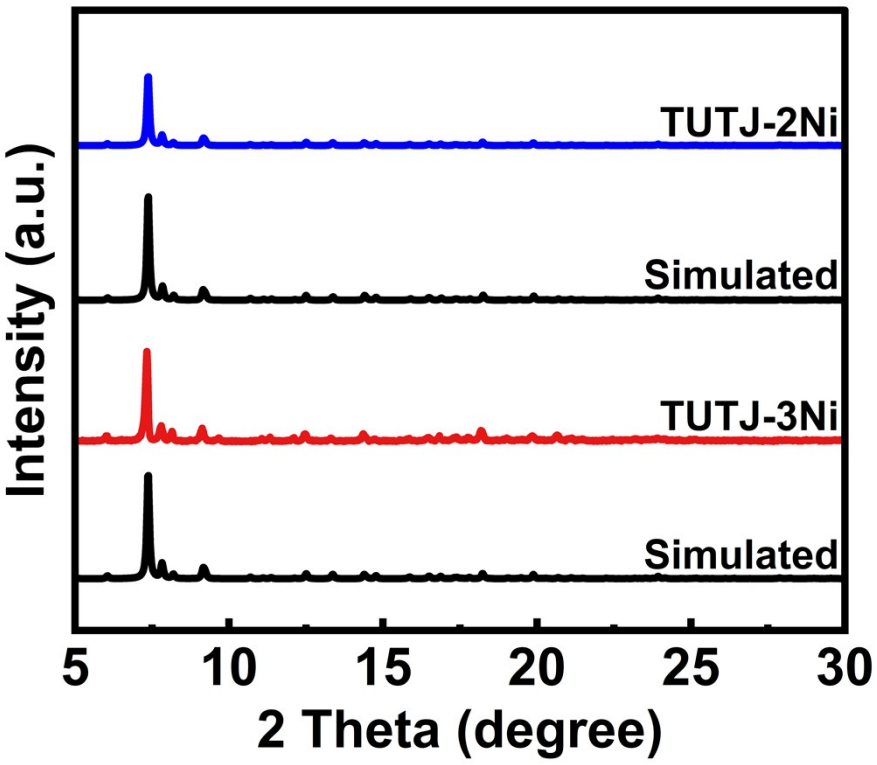

Figure S11. Experimental and simulated XRD patterns of TUTJ-2Ni and TUTJ-3Ni.

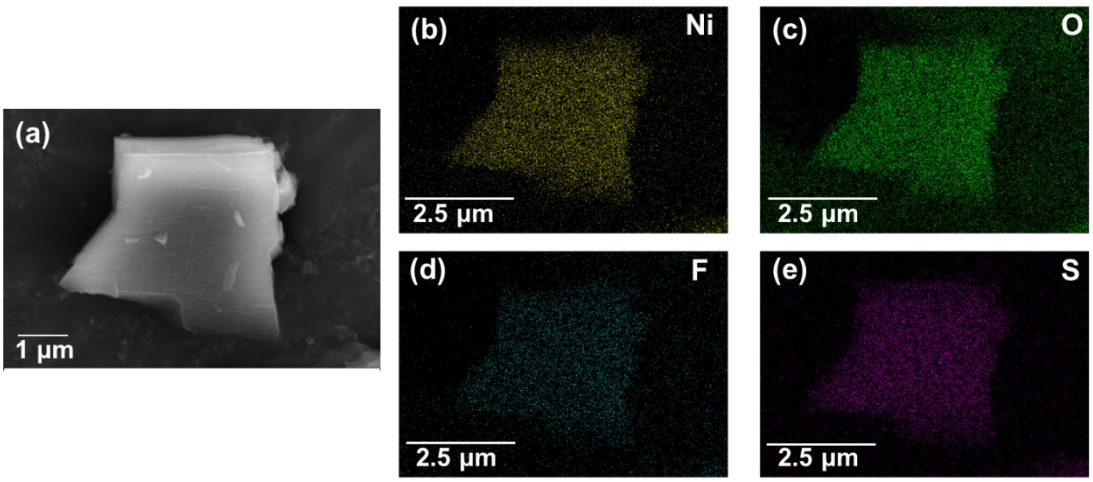

Figure S12. Morphology and elemental composition of TUTJ-2Ni. (a) SEM image and (b-e) corresponding elemental maps (Ni, O, F, S) demonstrating uniform distribution.

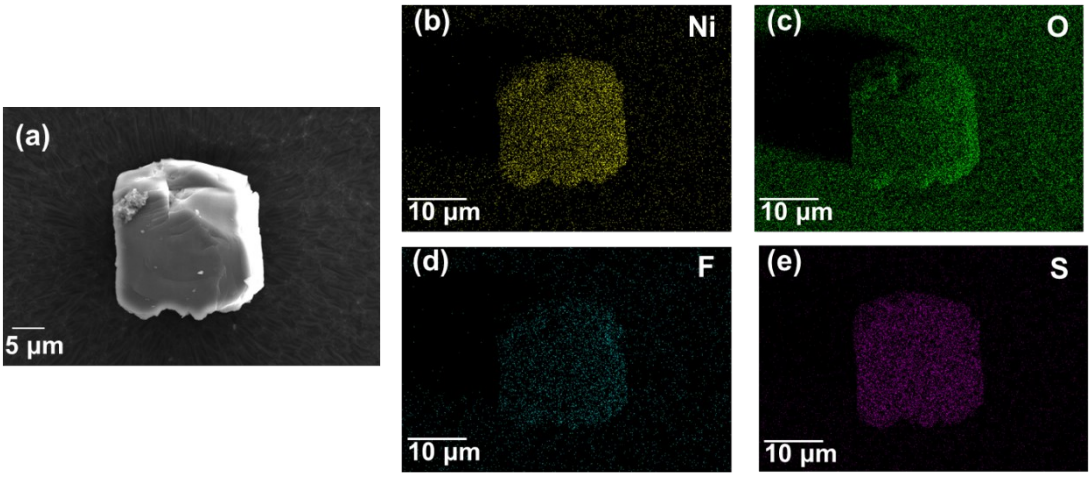

Figure S13. Morphology and elemental composition of TUTJ-3Ni. (a) SEM image and (b-e) corresponding elemental maps (Ni, O, F, S) demonstrating uniform distribution.

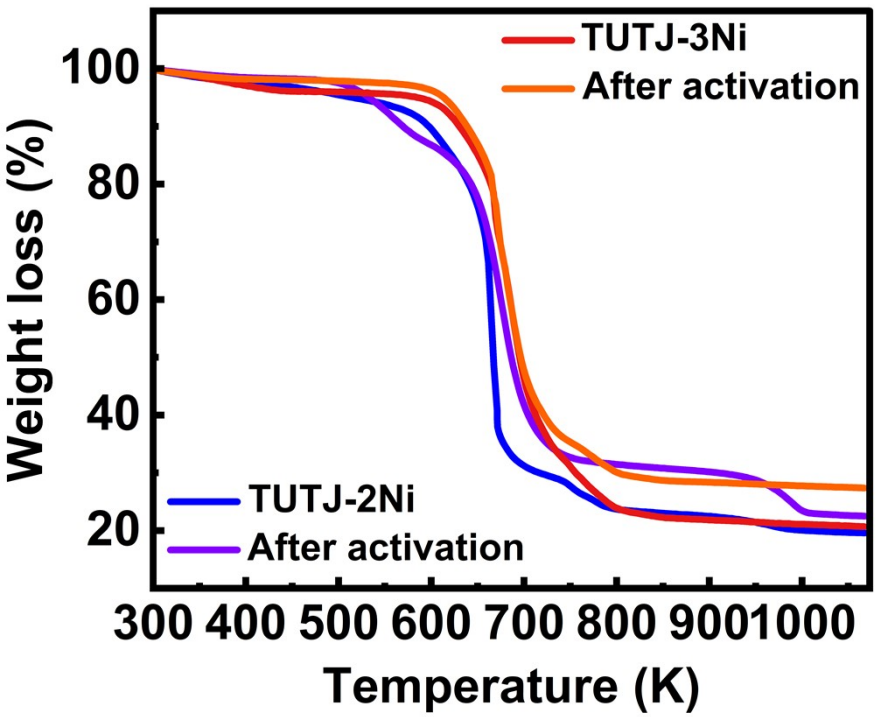

Figure S14. Thermogravimetric analysis curves of TUTJ-2Ni and TUTJ-3Ni before and after activation.

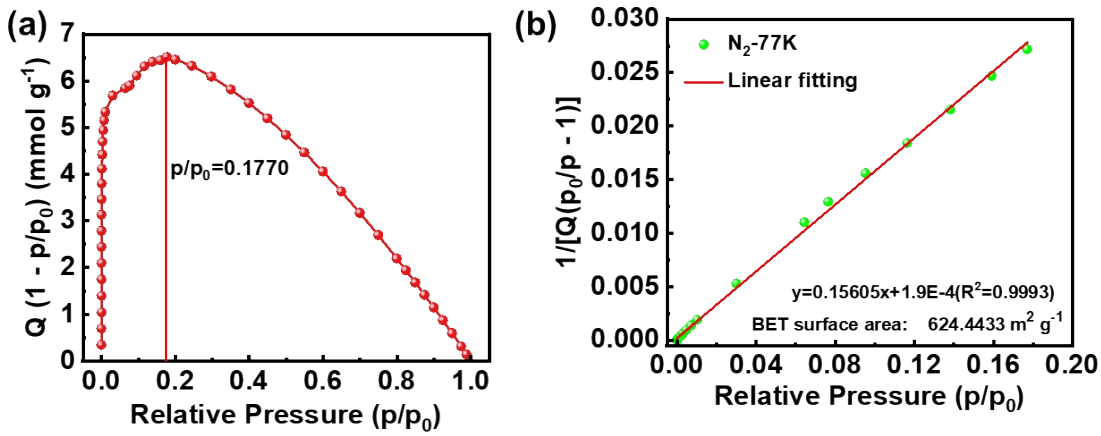

Figure S15. BET surface area determination for as-synthesized TUTJ-2Ni. (a) Plot of $V_{excess}(1 - P/P_0)$ vs. P/P_0 for the first consistency criterion. (b) Linear fit in the pressure range satisfying the second criterion, yielding the specific BET surface area.

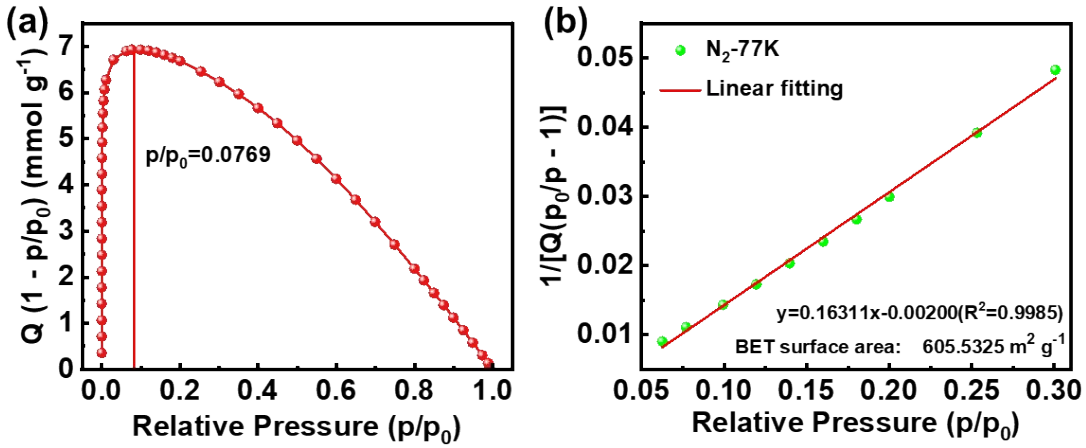

Figure S16. BET surface area determination for as-synthesized TUTJ-3Ni. (a) Plot of $V_{excess}(1 - P/P_0)$ vs. P/P_0 for the first consistency criterion. (b) Linear fit in the pressure range satisfying the second criterion, yielding the specific BET surface area.

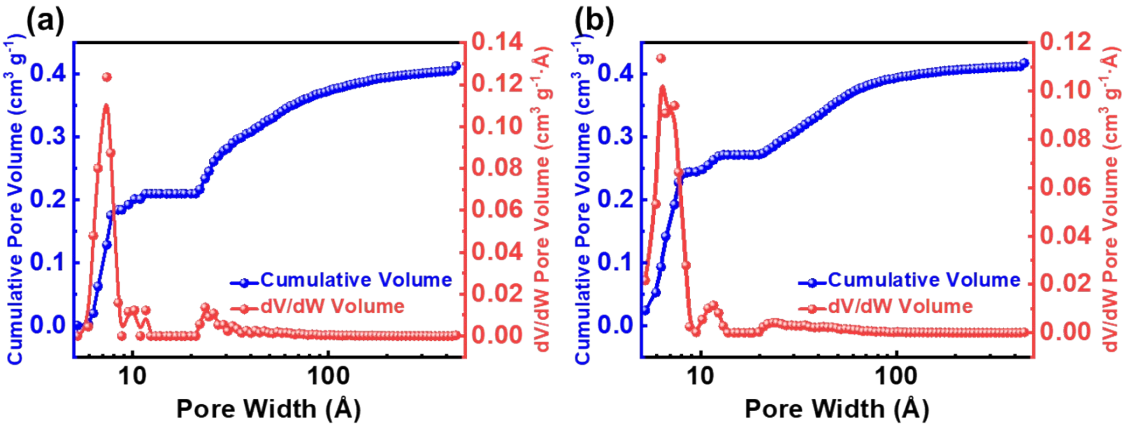

Figure S17. Logarithmic pore volume and pore size distribution of TUTJ-2Ni (a) and TUTJ-3Ni (b) by NLDFT model.

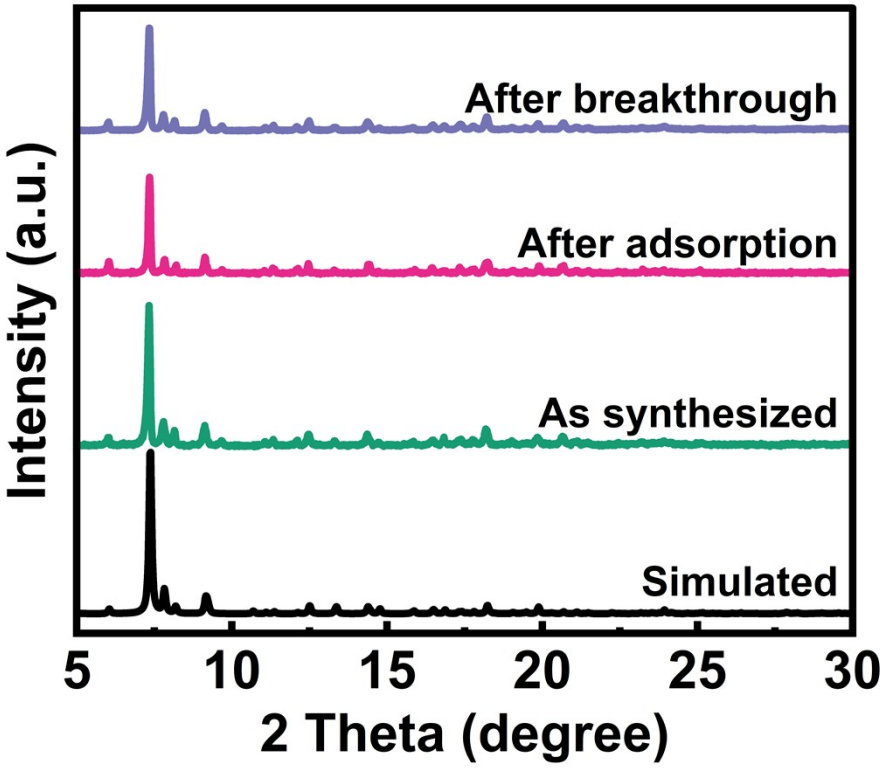

Figure S18. The PXRD patterns of as-synthesized, after-adsorption and after-breakthrough TUTJ-3Ni samples along with the simulated pattern from the single crystal X-ray structure.

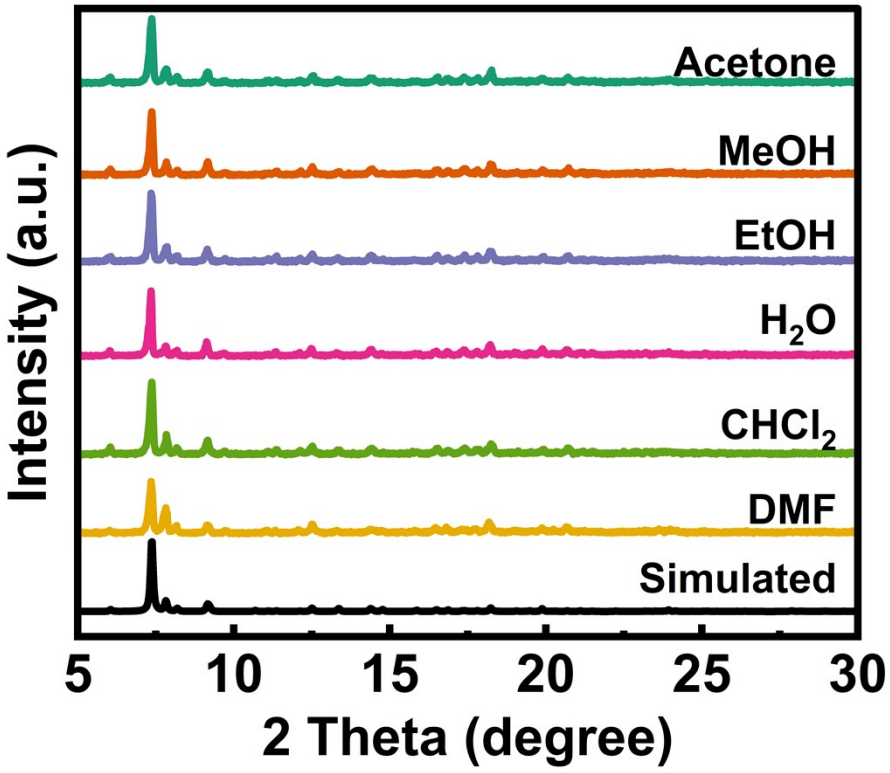

Figure S19. The PXRD patterns of TUTJ-3Ni soaking different solvents for two weeks.

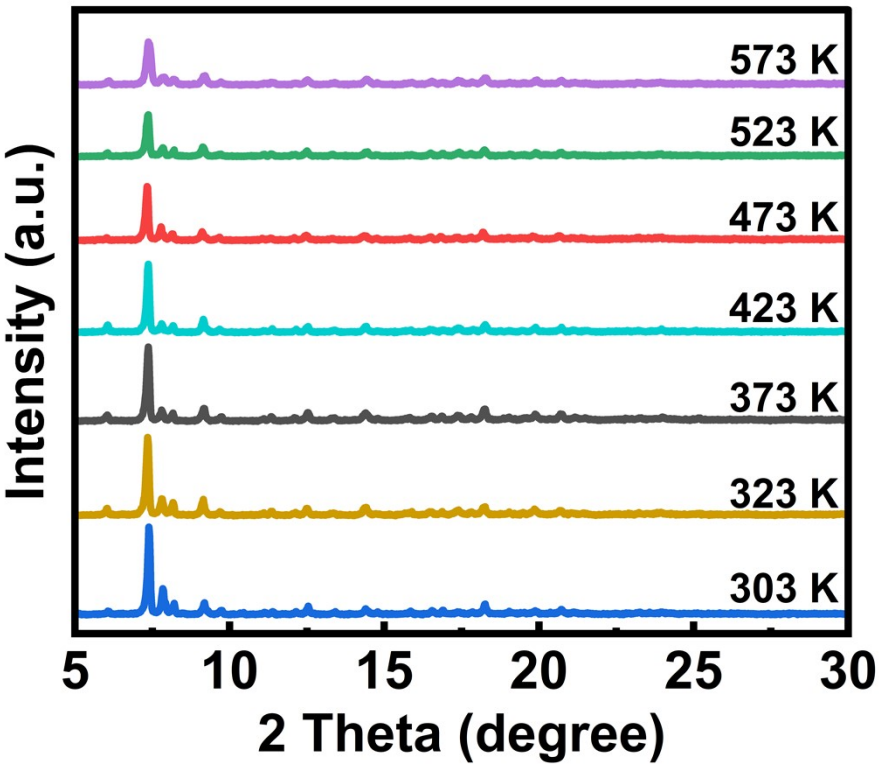

Figure S20. The PXRD patterns of TUTJ-3Ni after activation at different temperatures.

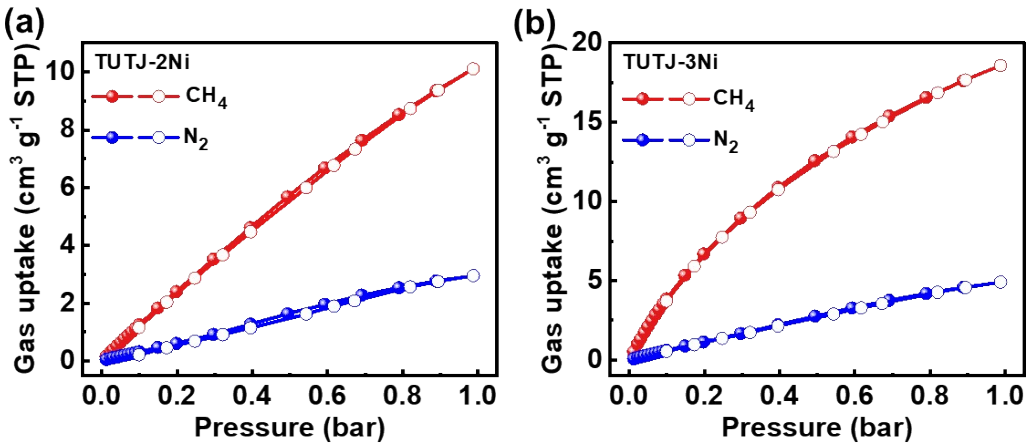

Figure S21. Gas sorption isotherms of TUTJ-2Ni (a) and TUTJ-3Ni (b) at 298 K. Adsorption (solid symbols) and desorption (open symbols) curves for CH_4 and N_2.

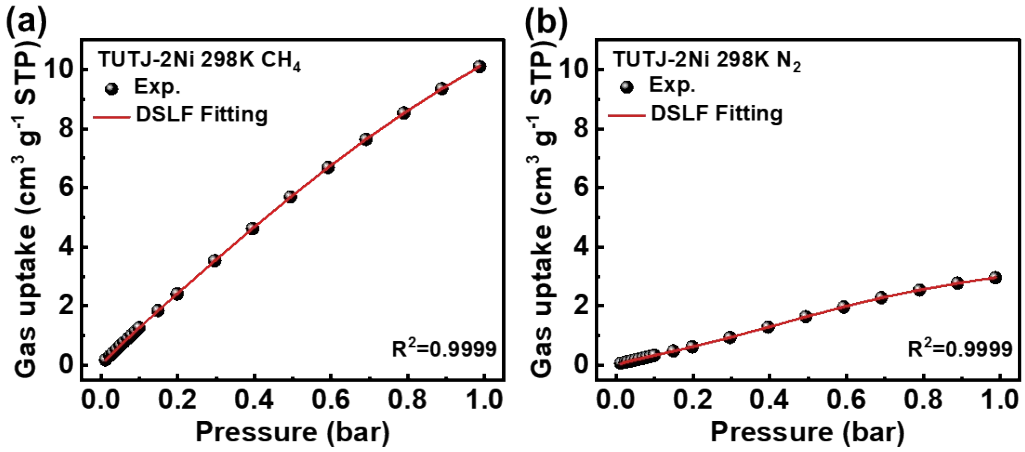

Figure S22. CH_4 (a) and N_2 (b) adsorption isotherms at 298 K in TUTJ-2Ni with dual-site Langmuir-Freundlich model fits (R-Square = 0.9999).

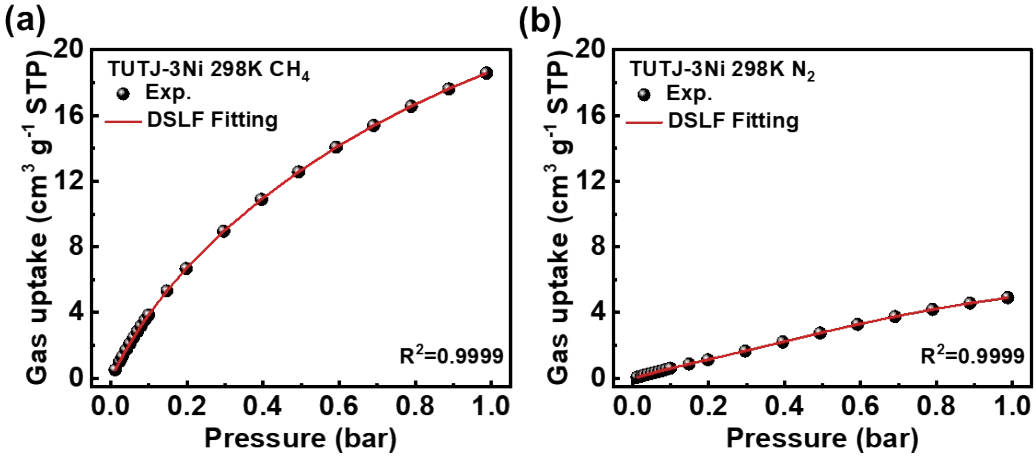

Figure S23. CH_4 (a) and N_2 (b) adsorption isotherms at 298 K in TUTJ-3Ni with dual-site Langmuir-Freundlich model fits (R-Square = 0.9999).

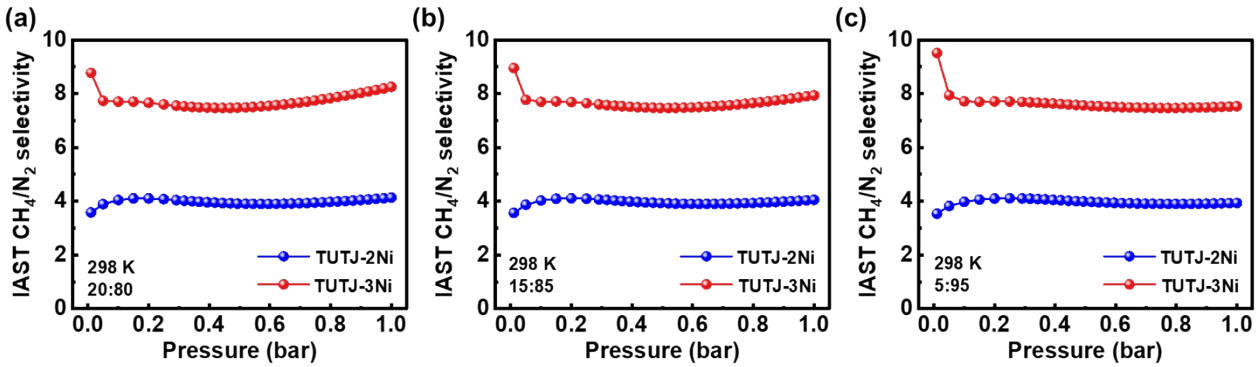

Figure S24. IAST selectivity at 298 K under CH_4/N_2 (20:80, 15:85, 5:95, v/v) mixture.

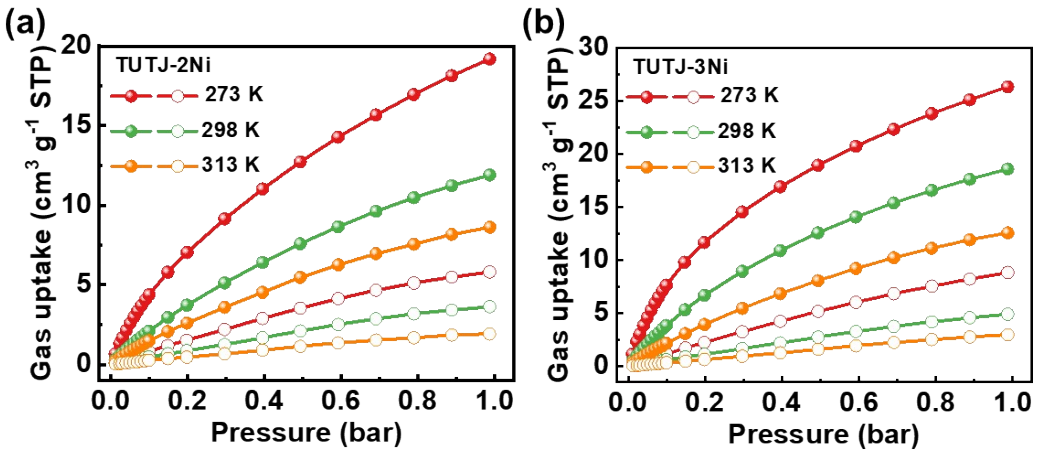

Figure S25. CH_4 and N_2 adsorption isotherms of TUTJ-2Ni (a) and TUTJ-3Ni (b) at 273 K, 298 K, and 313 K.

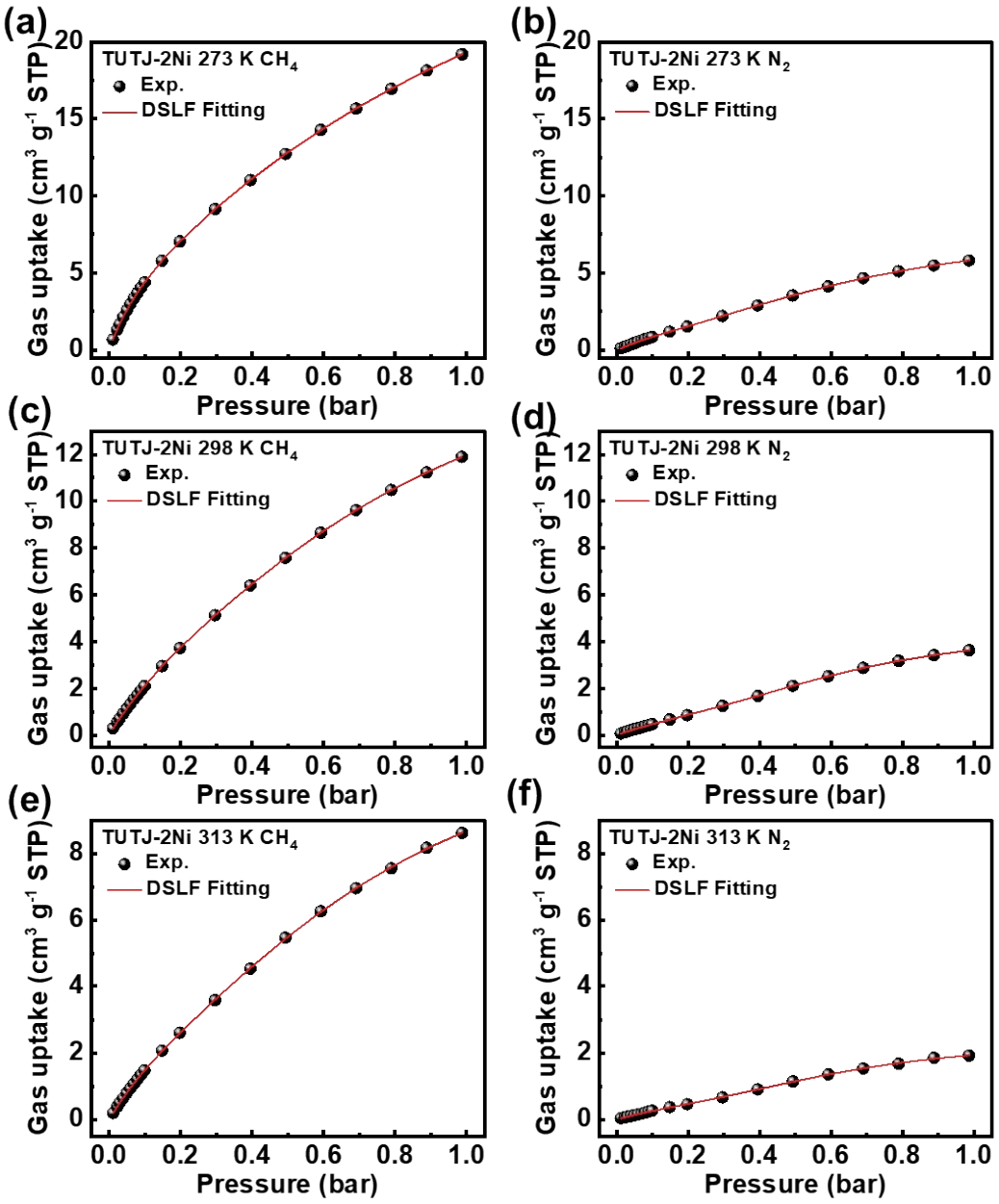

Figure S26. CH_4 and N_2 adsorption isotherms at 273 K(a,b), 298 K(c,d), and 313 K(e,f) in TUTJ-2Ni with dual-site Langmuir-Freundlich model fits (R-Square = 0.9999).

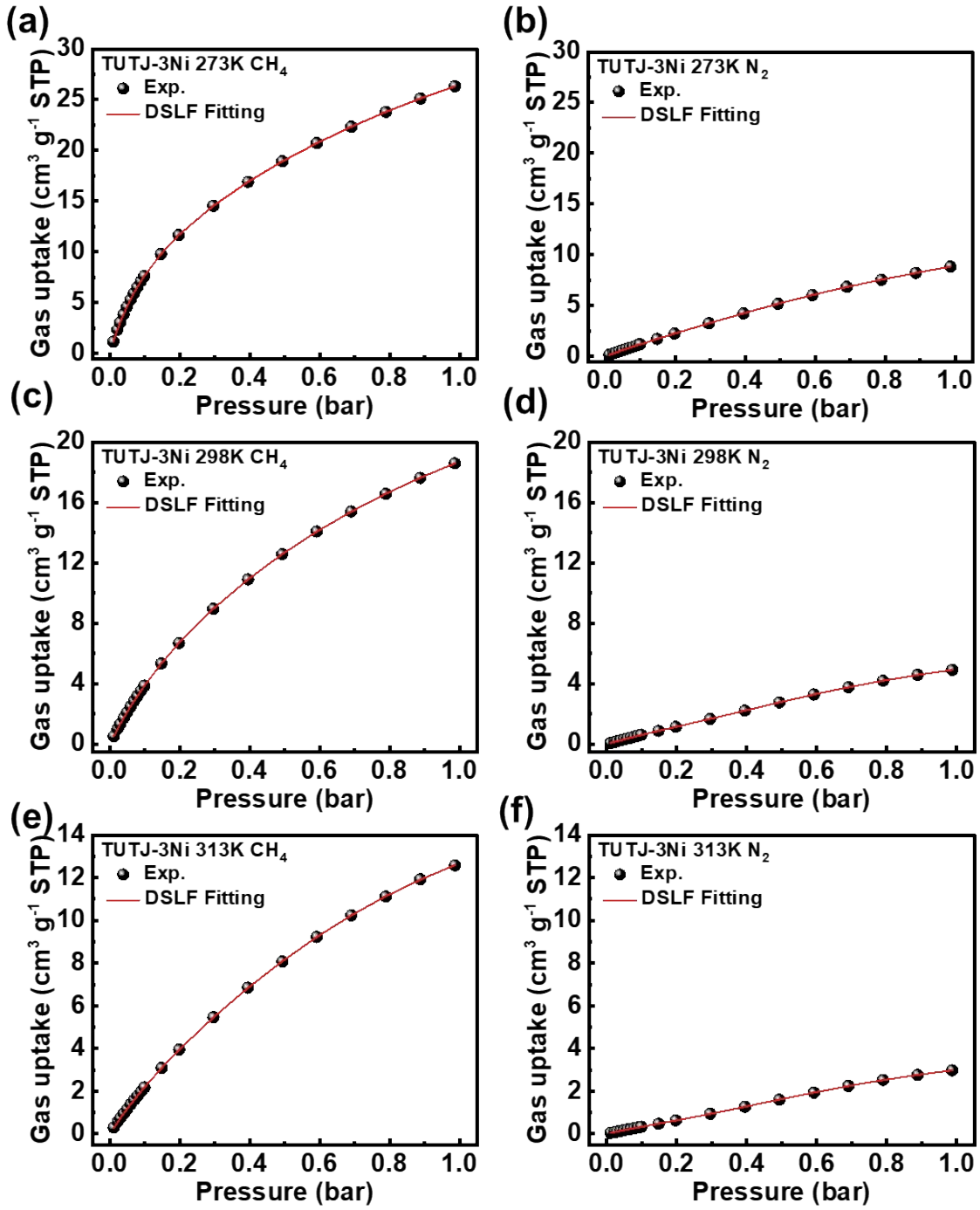

Figure S27. CH_4 and N_2 adsorption isotherms at 273 K(a,b), 298 K(c,d), and 313 K(e,f) in TUTJ-3Ni with dual-site Langmuir-Freundlich model fits (R-Square = 0.9999).

Table S3 The fitting parameters of the DSL model for CH_4 and N_2 adsorption on TUTJ-2Ni and TUTJ-3Ni.

Materials	Temperature (K)	Gas	q_1 ($cm^3\ g^{-1}$)	b_1 (bar^{-1})	n_1	q_2 ($cm^3\ g^{-1}$)	b_2 (bar^{-1})	n_2	R^2
TUTJ-2Ni	273	CH_4	23.13	0.91	0.64	9.54	6.83	0.99	0.9999
		N_2	5.82	2.26	0.47	2.06	7.38	0.90	0.9999
	298	CH_4	7.28	1.47	0.46	11.00	2.28	1.00	0.9999
		N_2	5.07	0.94	1.03	1.42	5.30	0.30	0.9999
	313	CH_4	3.72	6.74	0.90	8.76	1.64	0.52	0.9999
		N_2	1.67	3.20	0.38	0.76	6.91	0.84	0.9999
TUTJ-3Ni	273	CH_4	17.72	6.62	1.00	25.72	0.75	0.66	0.9999
		N_2	28.32	0.42	1.02	0.55	13.01	0.25	0.9999
	298	CH_4	18.45	0.87	0.68	13.06	3.47	1.00	0.9999
		N_2	5.85	1.54	0.48	1.59	7.39	0.85	0.9999
	313	CH_4	21.25	1.09	1.02	2.11	3.08	0.33	0.9999
		N_2	4.90	0.65	1.03	1.48	2.56	0.35	0.9999

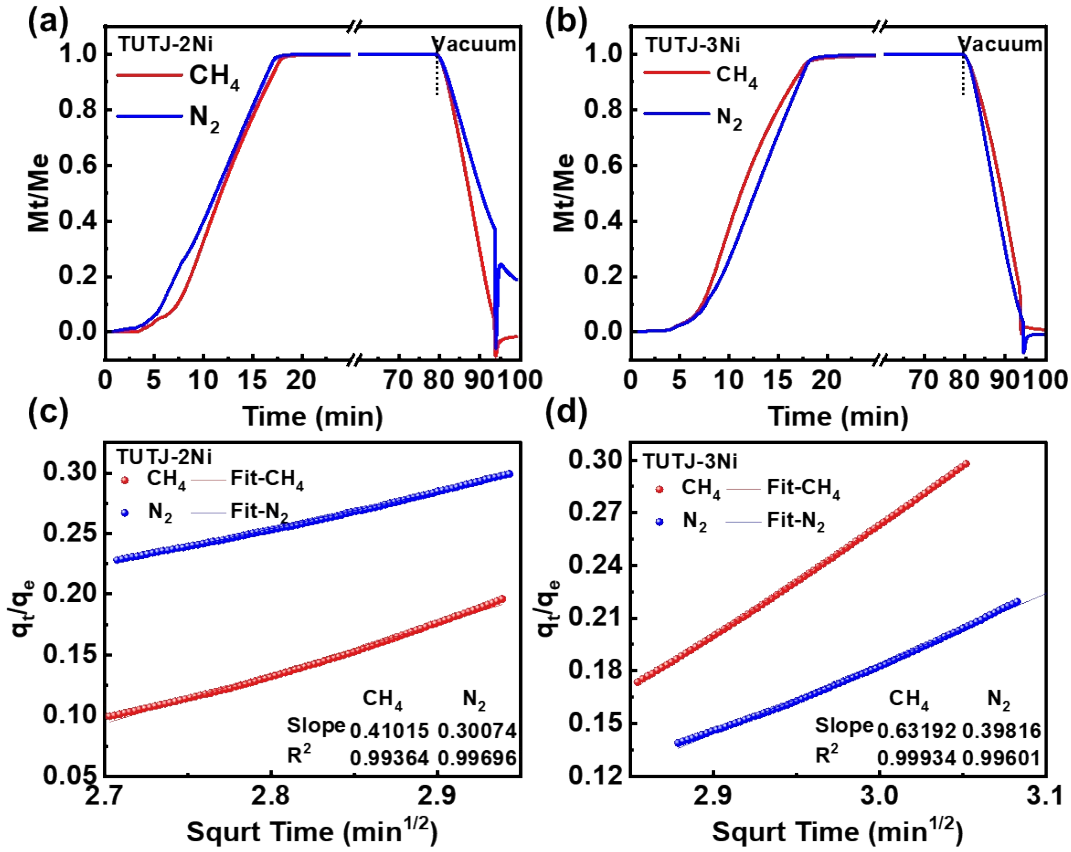

Figure S28. Kinetic adsorption/desorption profiles of CH_4 and N_2 for TUTJ-2Ni (a) and TUTJ-3Ni (b); Diffusional time constant calculation details for TUTJ-2Ni (c) and TUTJ-3Ni (d)at 298 K.

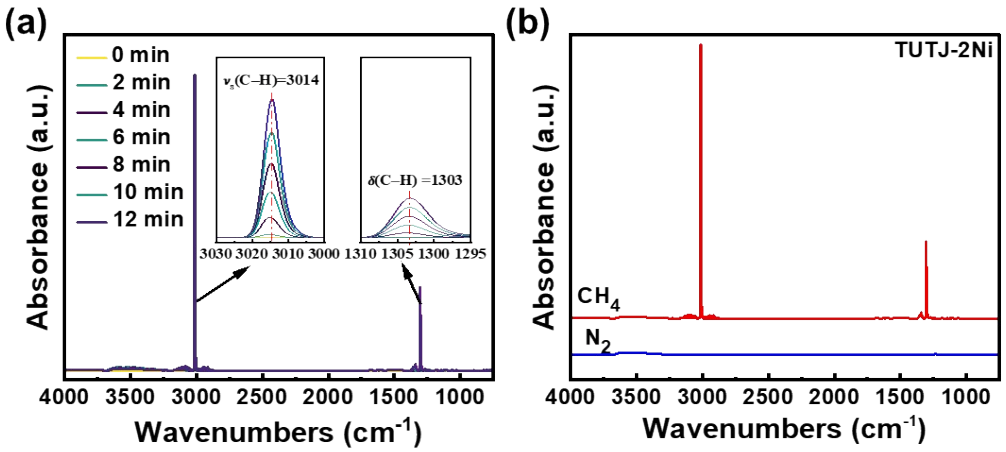

Figure S29. (a) In situ FTIR spectra of CH_4-loaded TUTJ-2Ni. The inset shows a magnified view of the characteristic region. (b) Comparison of in situ FTIR spectra for TUTJ-2Ni loaded with CH_4 and N_2.

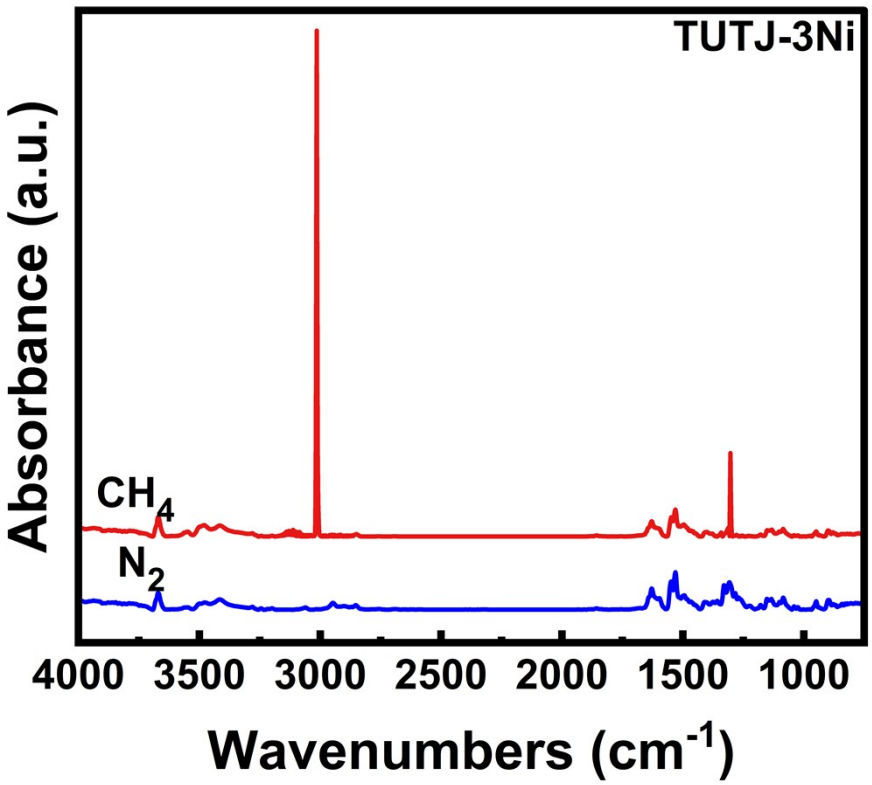

Figure S30. Comparison of in situ FTIR spectra for TUTJ-3Ni loaded with CH_4 and N_2.

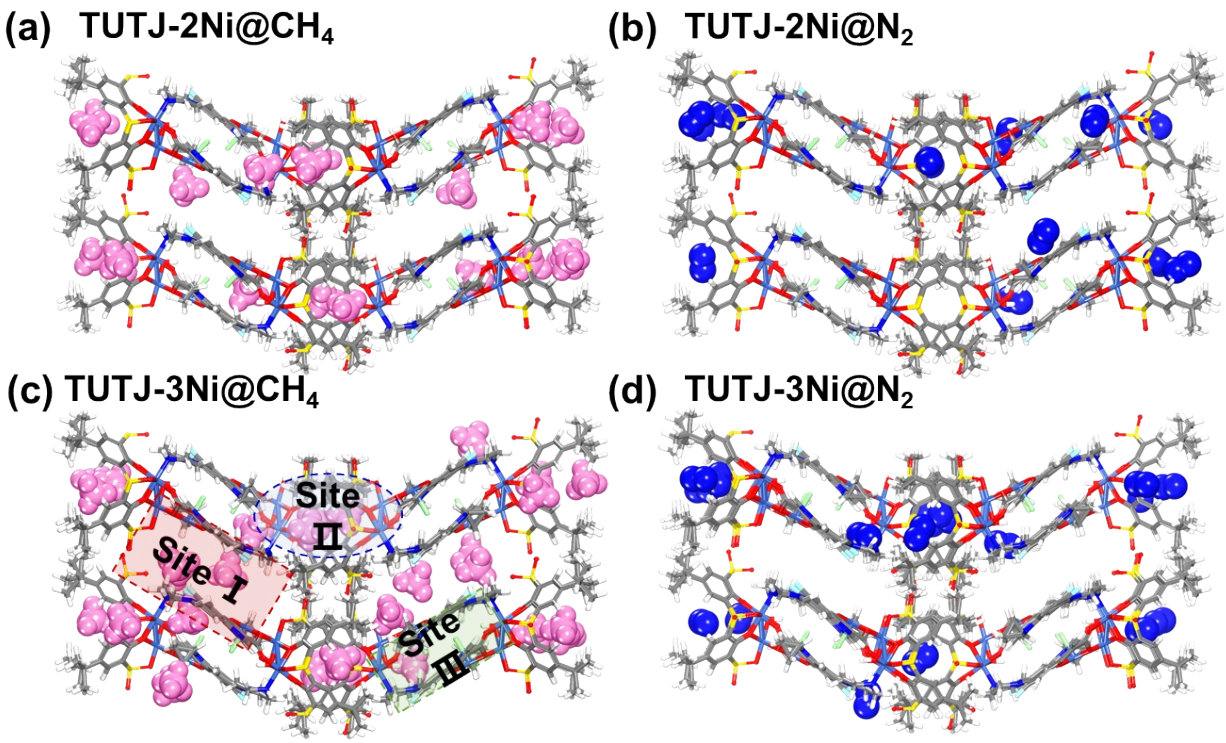

Figure S31. GCMC-derived probability density distributions for adsorbed CH_4 and N_2 molecules in TUTJ-2Ni (a, b) and TUTJ-3Ni (c, d) at 298 K and 1.0 bar, respectively.

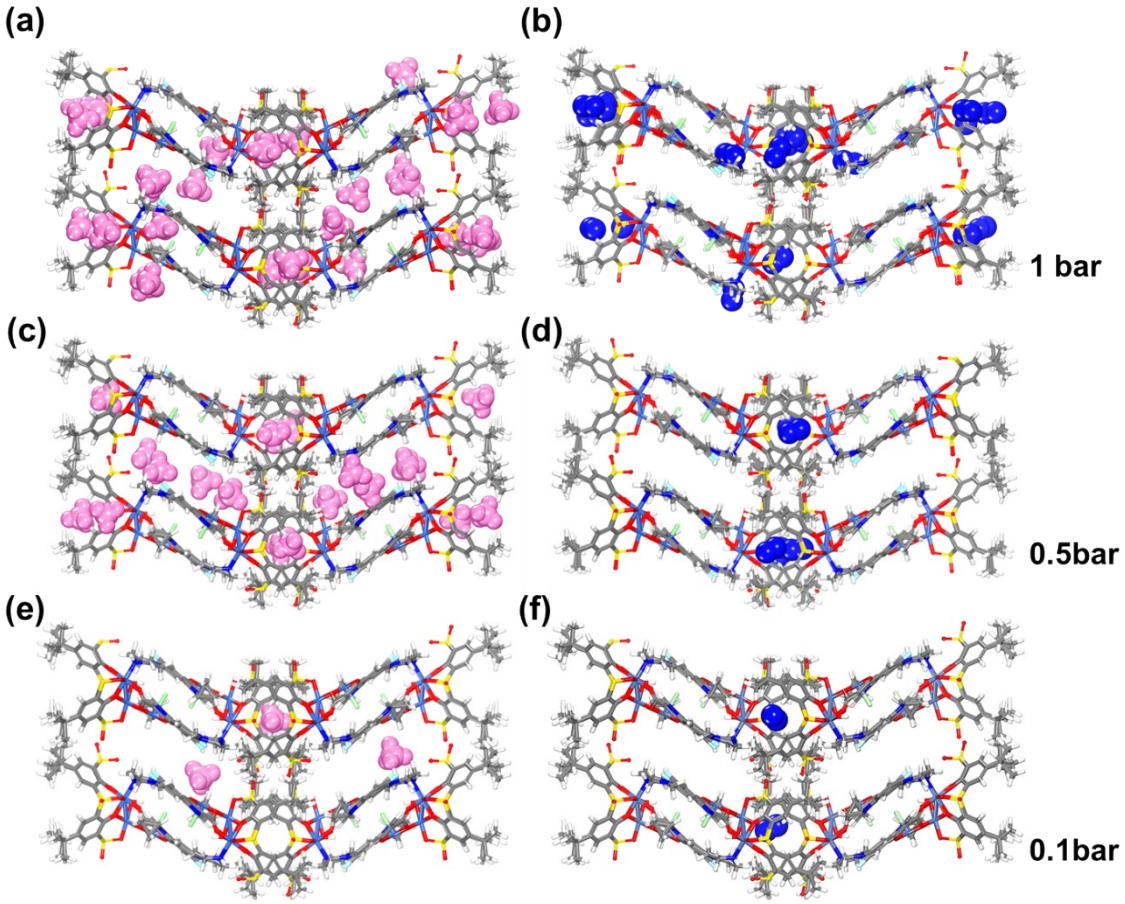

Figure S32. GCMC-derived probability density distributions for adsorbed CH_4 and N_2 molecules in TUTJ-3Ni at 298 K and 0.1-1.0 bar, respectively.

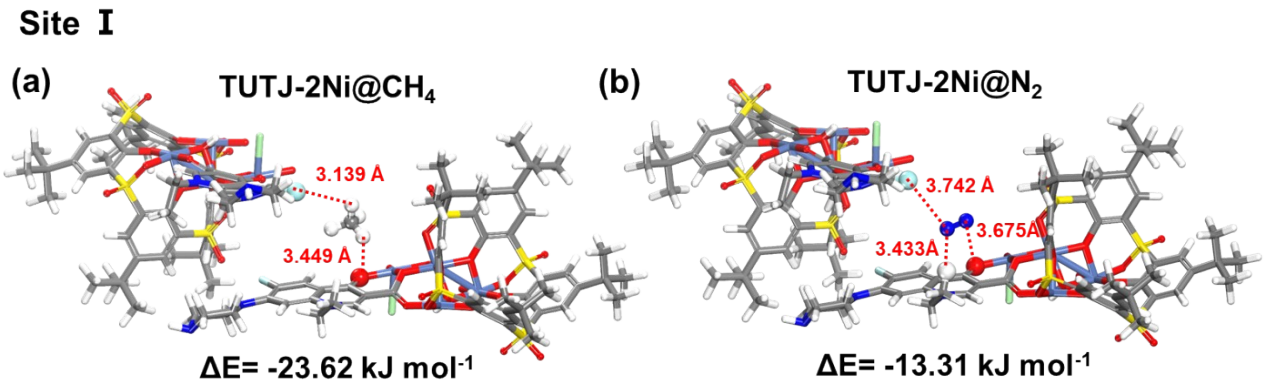

Figure S33. DFT-optimized adsorption configurations of (d) CH_4 and (e) N_2 molecules in TUTJ-2Ni.

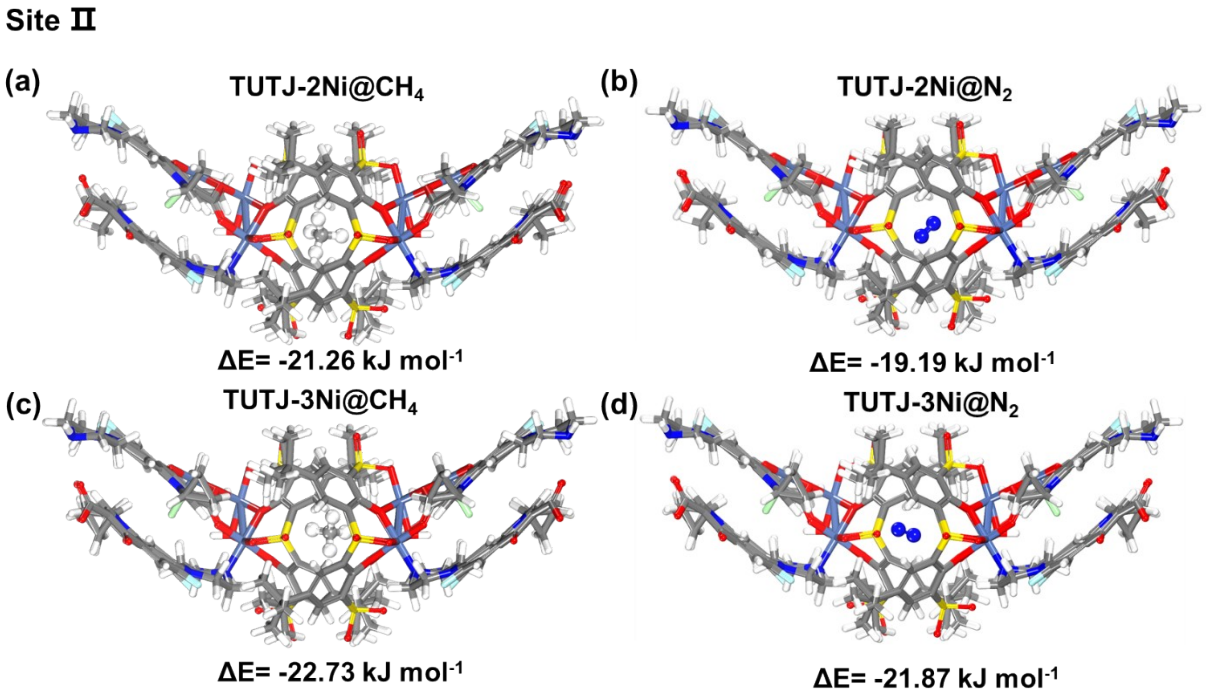

Figure S34. The DFT optimized adsorption configurations of CH_4 molecules and N_2 molecules at site II in TUTJ-2Ni and TUTJ-3Ni materials.

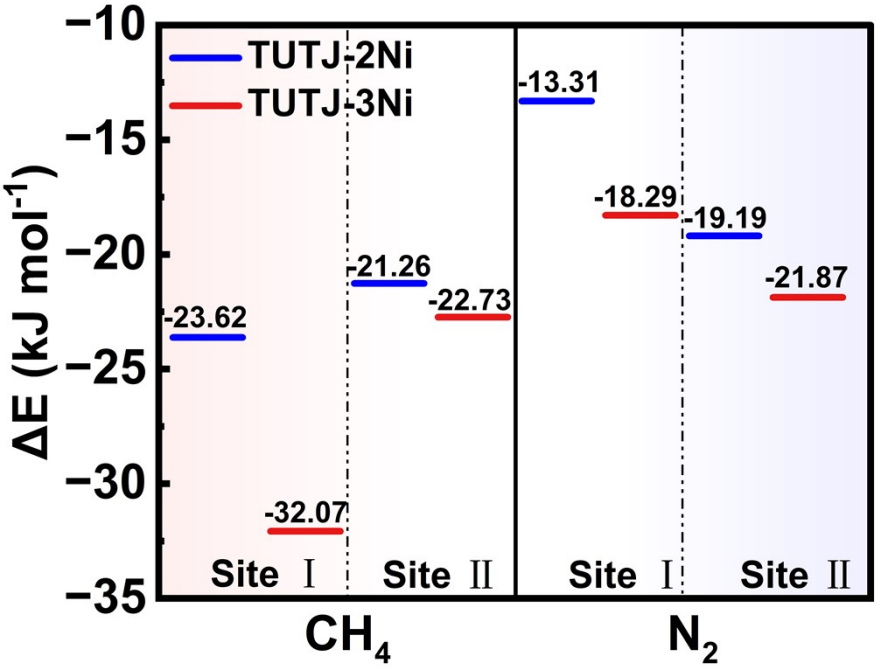

Figure S35. Adsorption energy ΔE of TUTJ-2Ni and TUTJ-3Ni.

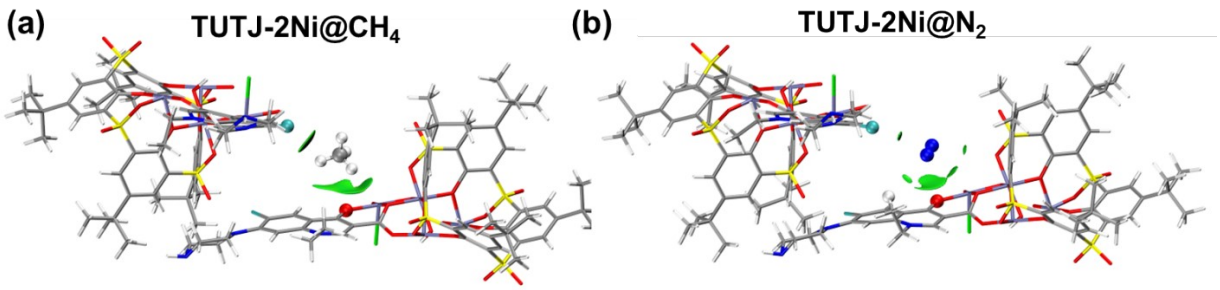

Figure S36. IGMH isosurfaces (isovalue = 0.002 a.u.) for (a) CH_4 and (b) N_2 on TUTJ-2Ni, where the green regions denote vdW-type interactions.

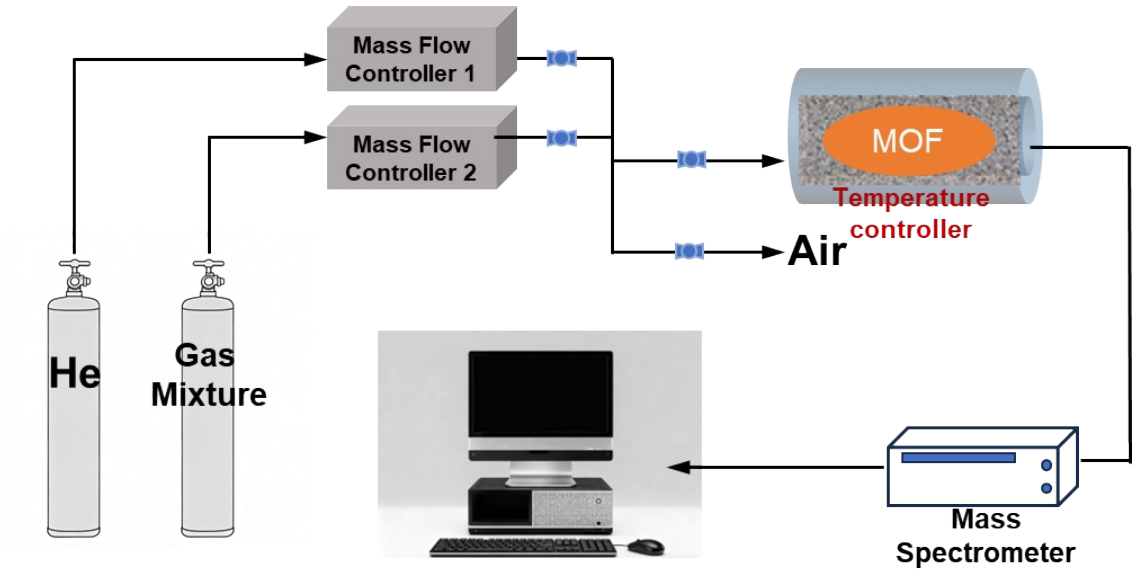

Figure S37. Schematic illustration of the setup for breakthrough experiments.

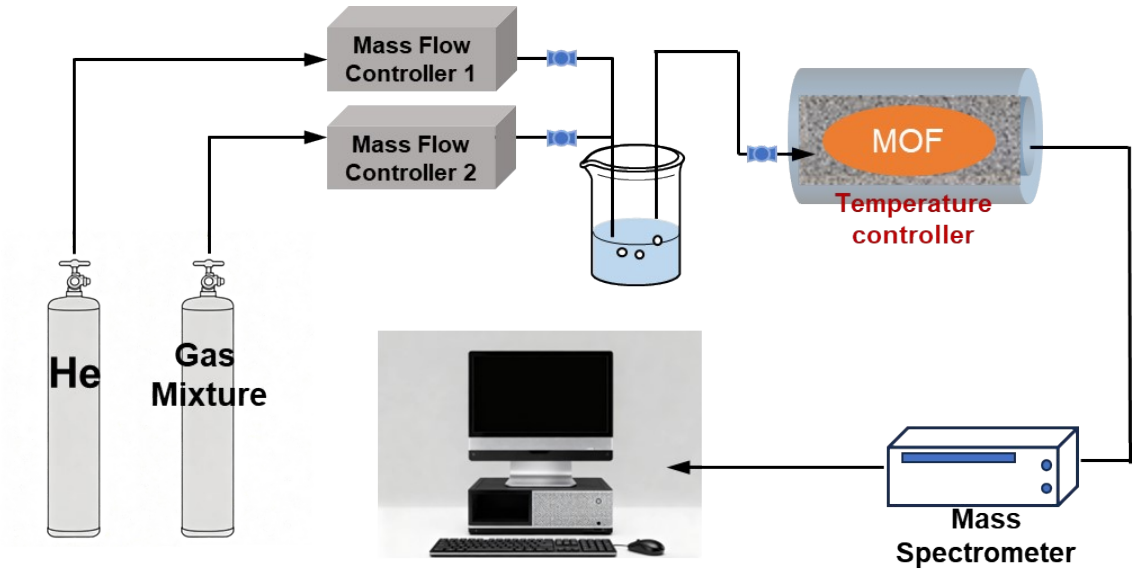

Figure S38. Schematic illustration of the apparatus for the breakthrough experiments under humid conditions.

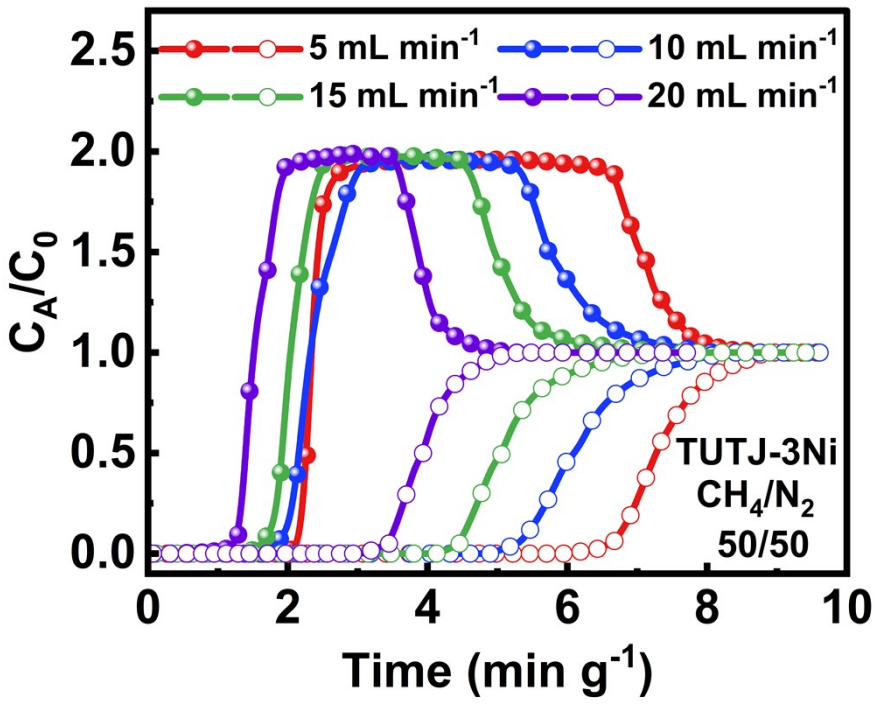

Figure S39. Breakthrough curves for TUTJ-3Ni under a 50:50 CH_4/N_2 mixture at varying flow rates.

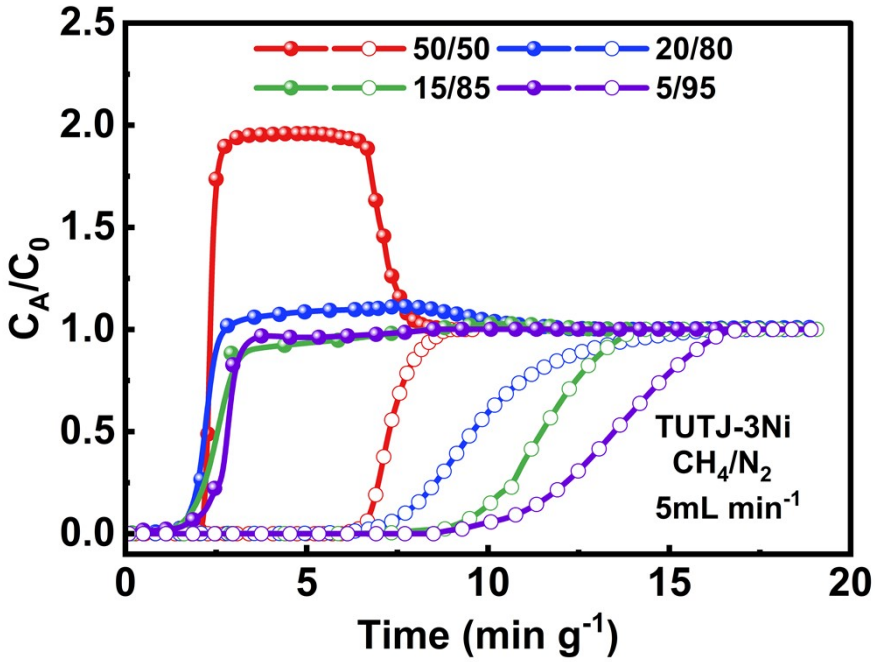

Figure S40. Breakthrough curves of TUTJ-3Ni for CH_4/N_2 mixtures with different ratios at a total flow rate of 5 mL min^{-1}.

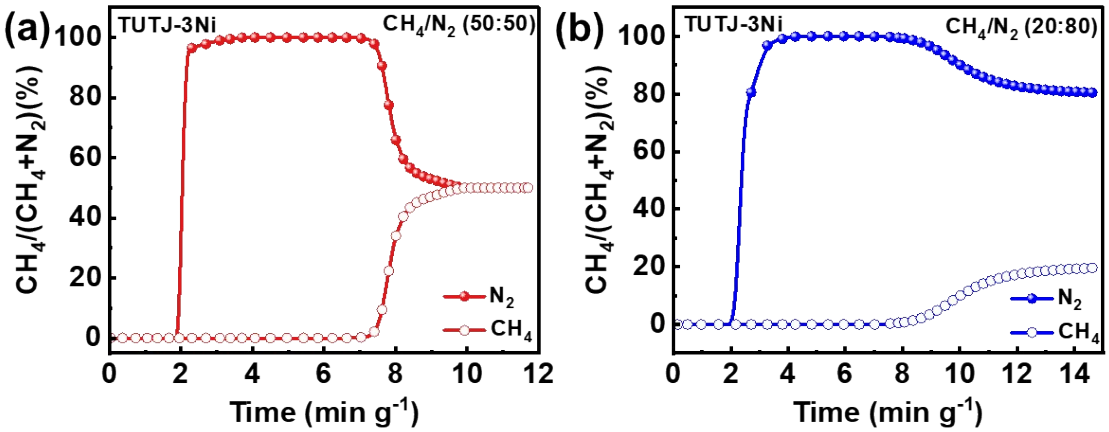

Figure S41. Breakthrough curves of TUTJ-3Ni for 50:50 and 20:80 CH_4/N_2 mixtures.

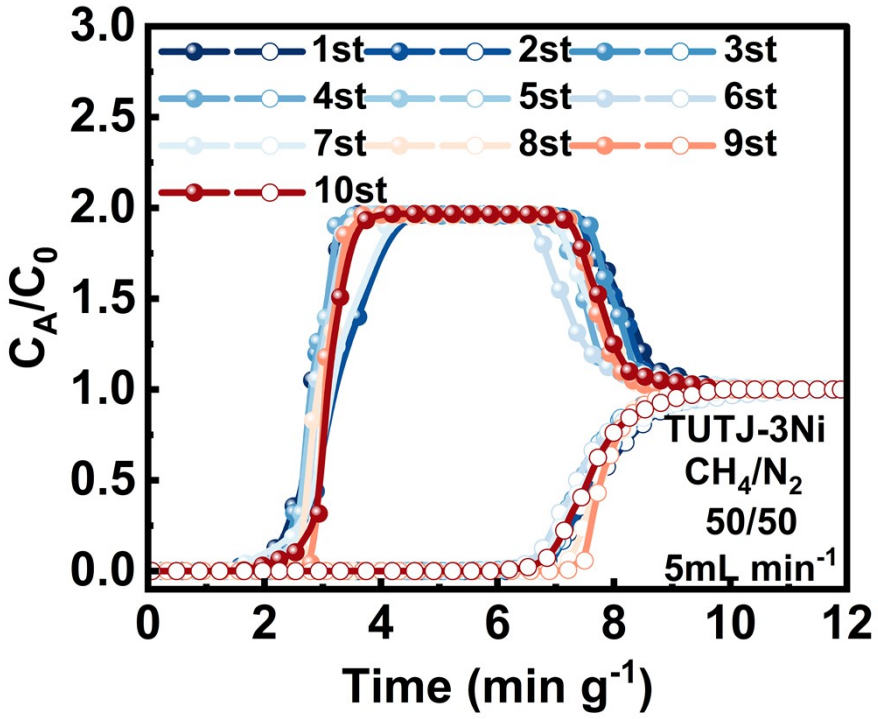

Figure S42. Ten consecutive CH_4/N_2 (50:50) breakthrough cycles for TUTJ-3Ni at a flow rate of 5 mL min^{-1}.

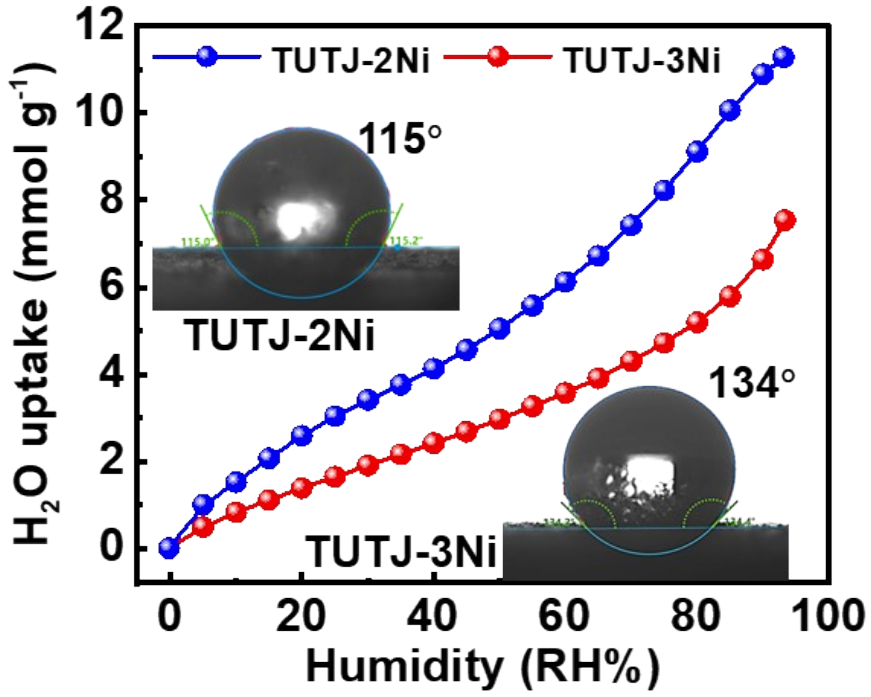

Figure S43. Water vapor adsorption isotherms of TUTJ-2Ni and TUTJ-3Ni at 298 K. The insets show the water contact angle.

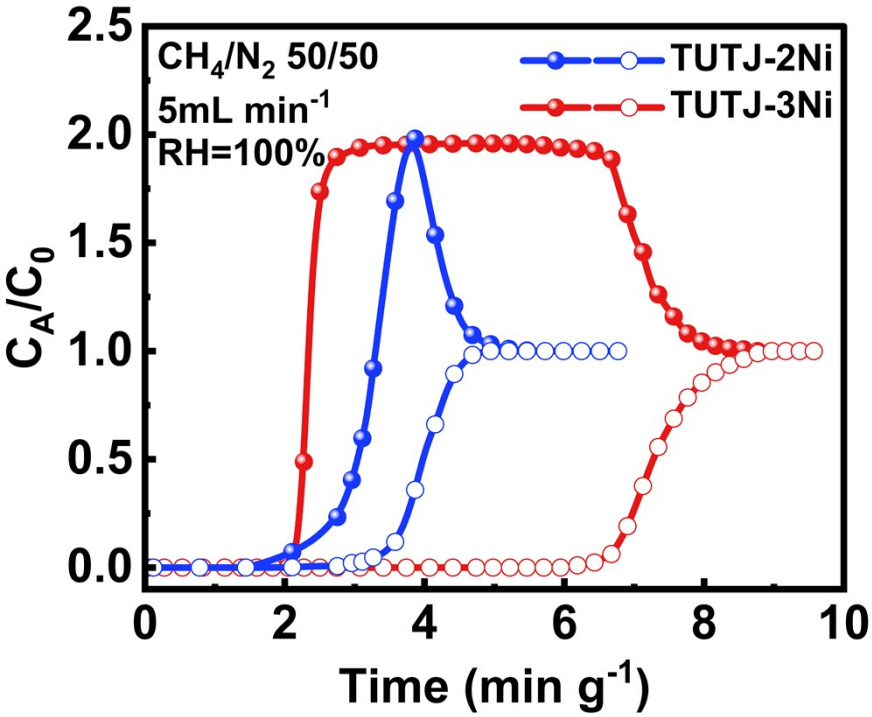

Figure S44. Breakthrough curves of TUTJ-2Ni and TUTJ-3Ni for a 50:50 CH_4/N_2 mixture under 100% relative humidity at a total flow rate of 5 mL min^{-1}.

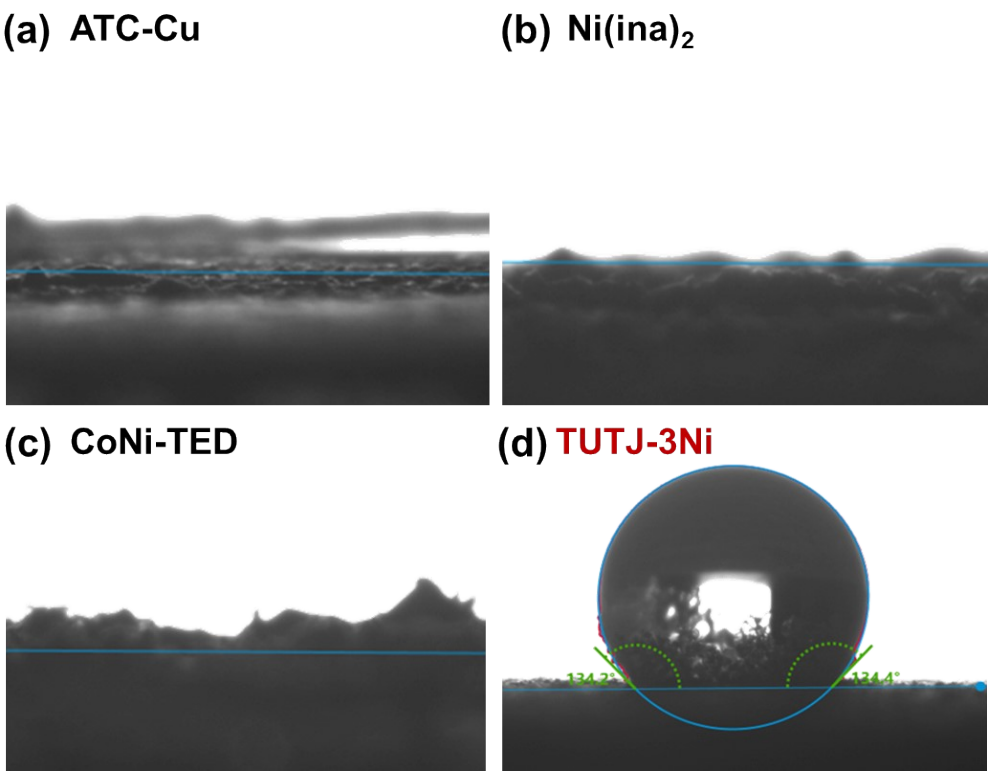

Figure S45. Water contact angles of ATC-Cu (a), $Ni(ina)_2$ (b), CoNi-TED (c), and TUTJ-3Ni (d).

Figure S46. Photograph of a water droplet on a compacted pellet of TUTJ-3Ni.

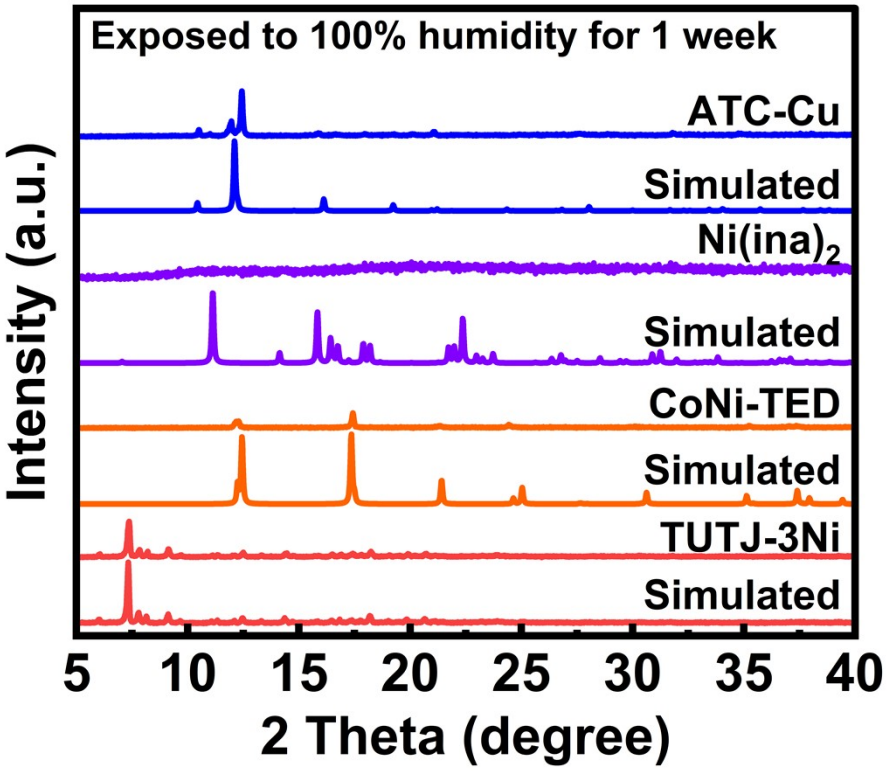

Figure S47. PXRD patterns of ATC-Cu, $Ni(ina)_2$, CoNi-TED, and TUTJ-3Ni after one-week exposure to 100% RH.

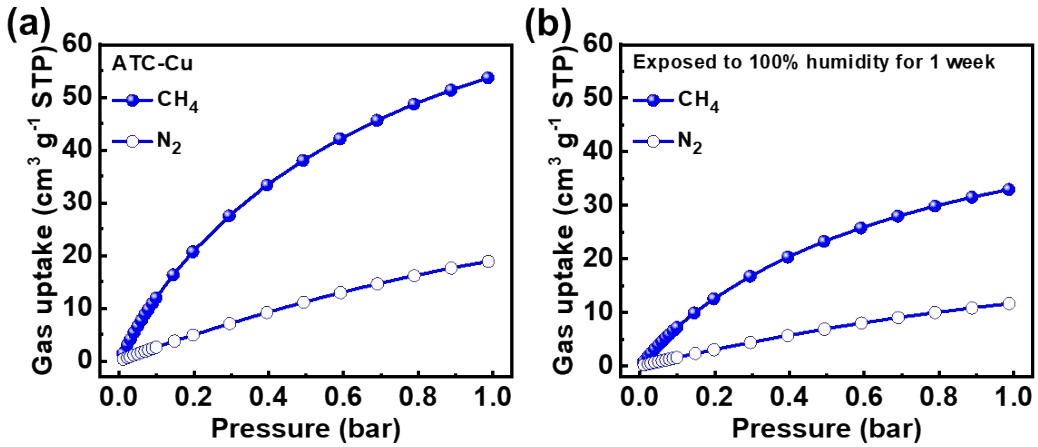

Figure S48. CH_4 and N_2 sorption isotherms of ATC-Cu (pristine and exposure to 100% RH for 1 week).

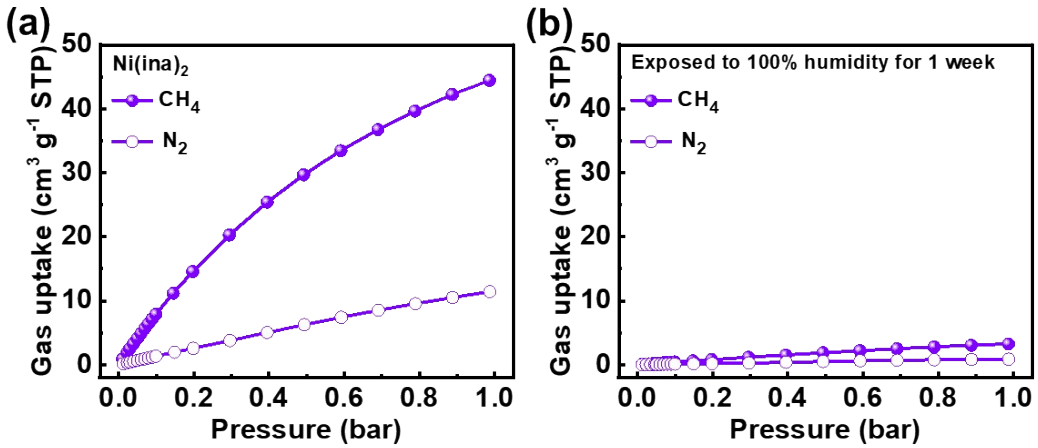

Figure S49. CH_4 and N_2 sorption isotherms of $Ni(ina)_2$ (pristine and exposure to 100% RH for 1 week).

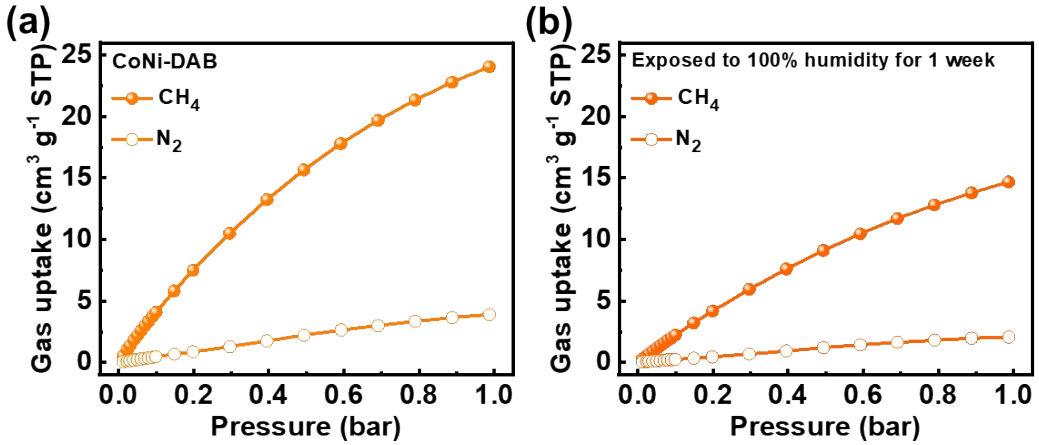

Figure S50. CH_4 and N_2 sorption isotherms of CoNi-TED (pristine and exposure to 100% RH for 1 week).

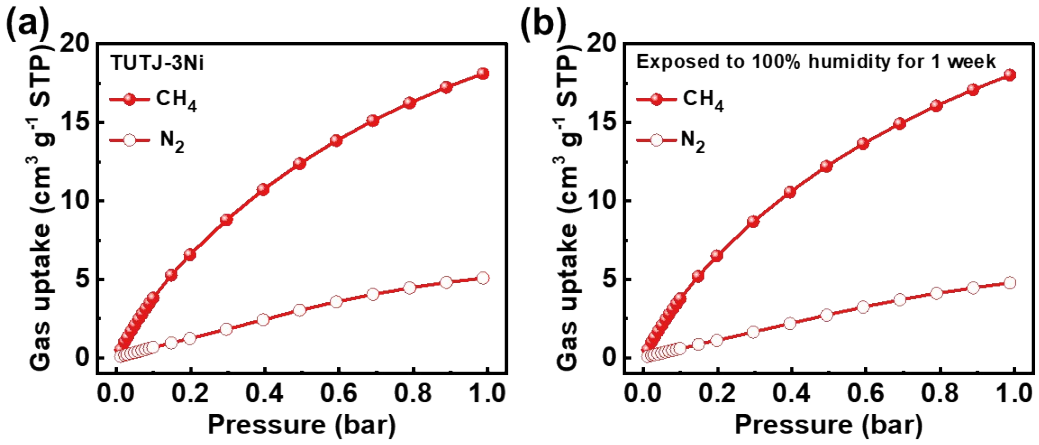

Figure S51. CH_4 and N_2 sorption isotherms of TUTJ-3Ni (pristine and exposure to 100% RH for 1 week).

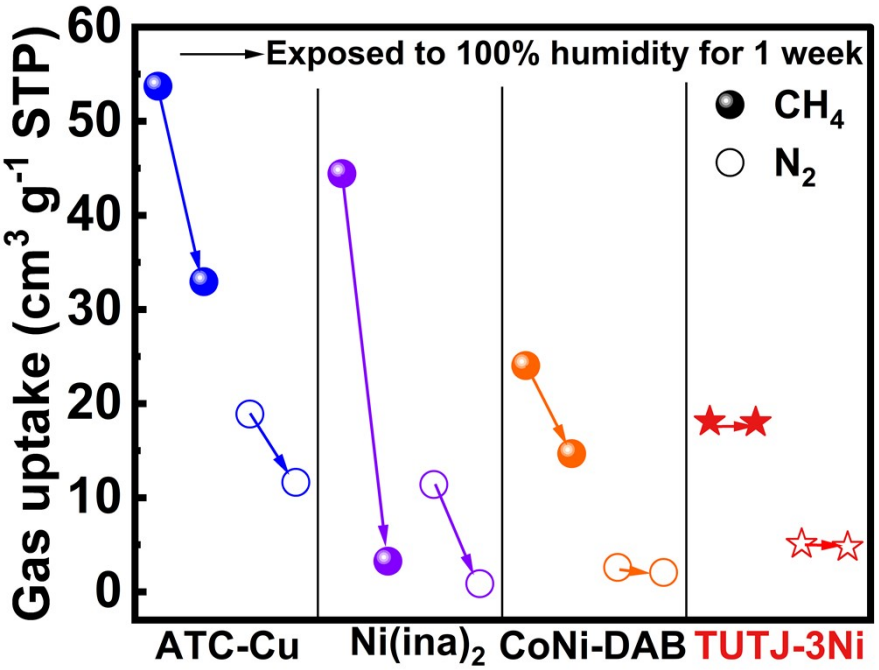

Figure S52. CH_4 and N_2 uptakes at 1 bar and 298 K before and after exposure to 100% RH.

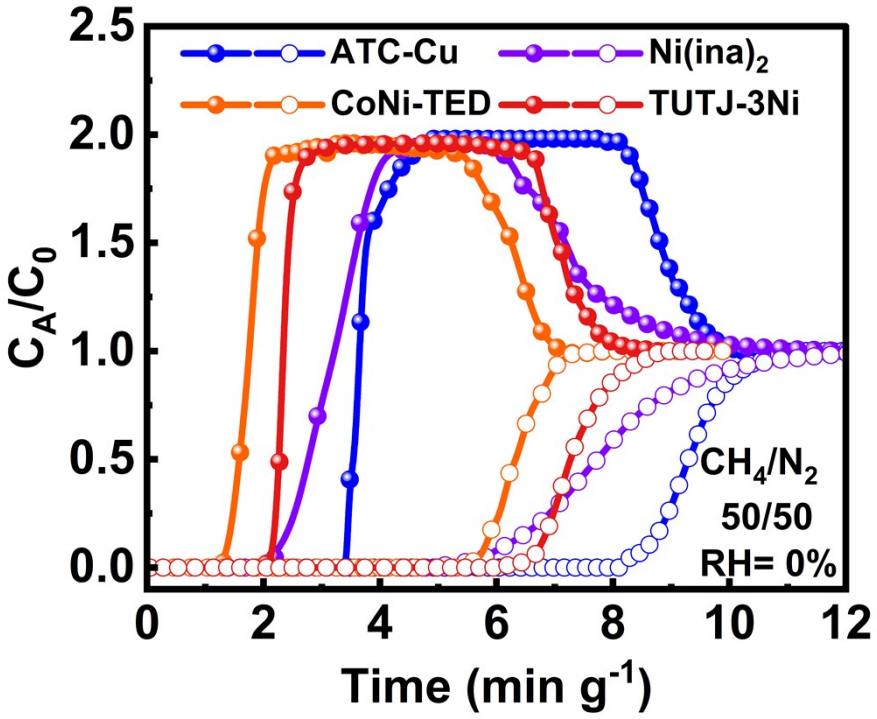

Figure S53. Breakthrough curves under dry CH_4/N_2 (50:50) flow.

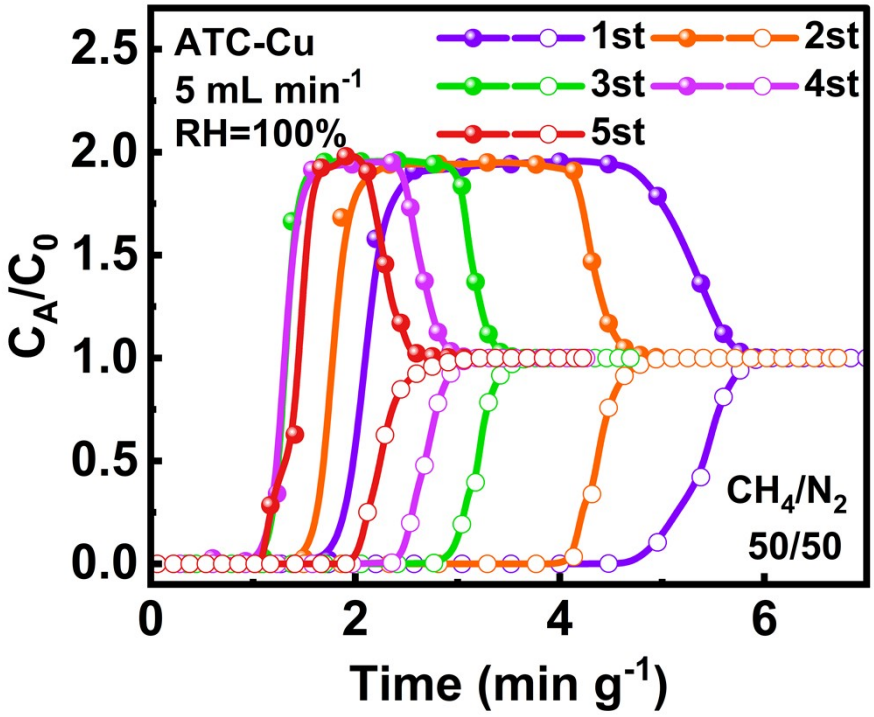

Figure S54. Breakthrough curves of ATC-Cu over five consecutive cycles under 100% relative humidity.

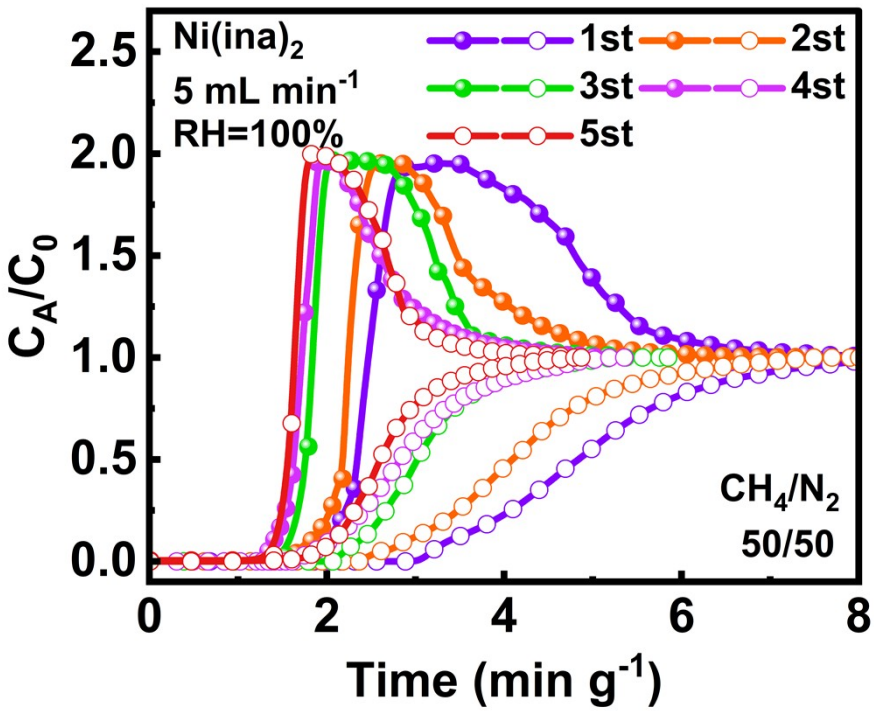

Figure S55. Breakthrough curves of $Ni(ina)_2$ over five consecutive cycles under 100% relative humidity.

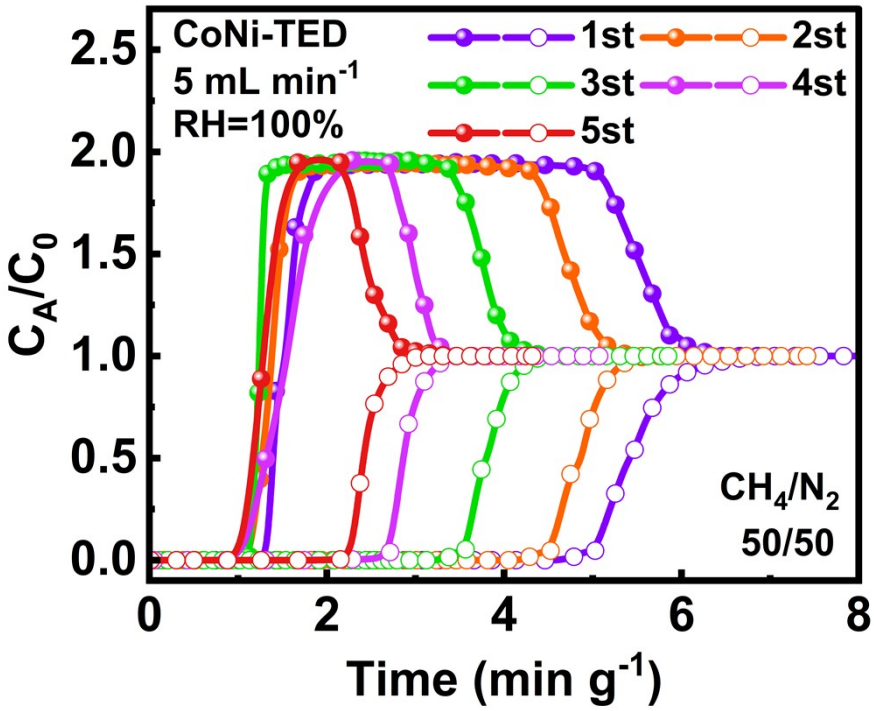

Figure S56. Breakthrough curves of CoNi-TED over five consecutive cycles under 100% relative humidity.

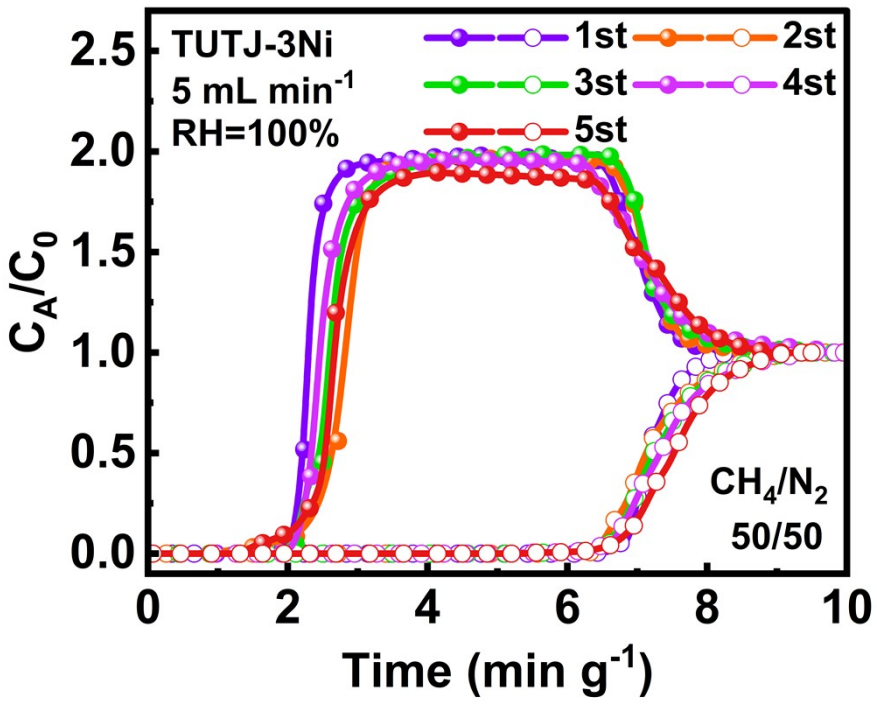

Figure S57. Breakthrough curves of TUTJ-3Ni over five consecutive cycles under 100% relative humidity.

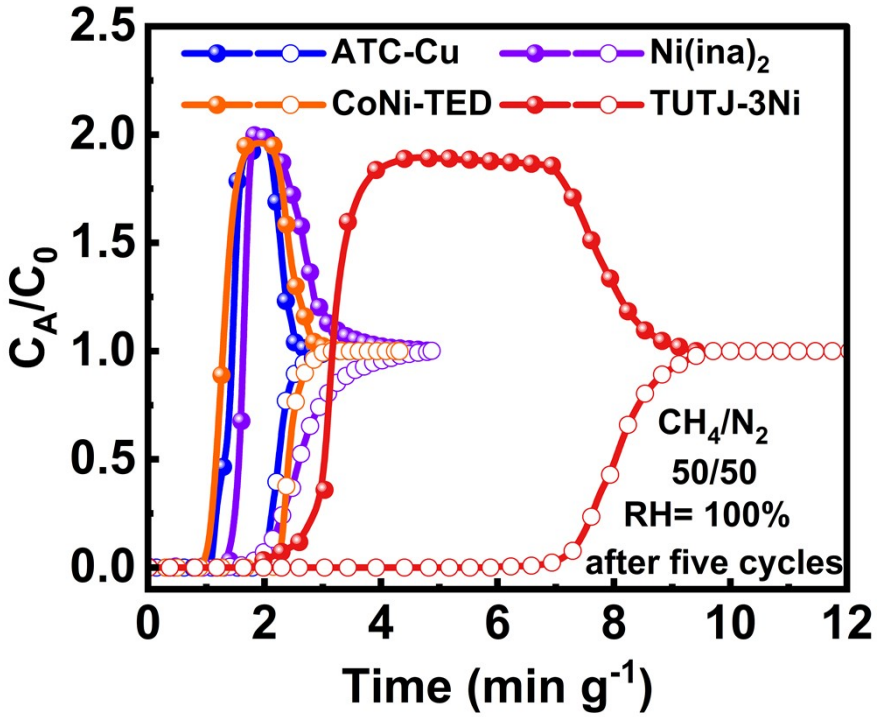

Figure S58. Fifth breakthrough cycles under humid (RH = 100%) CH_4/N_2 (50:50) flow.

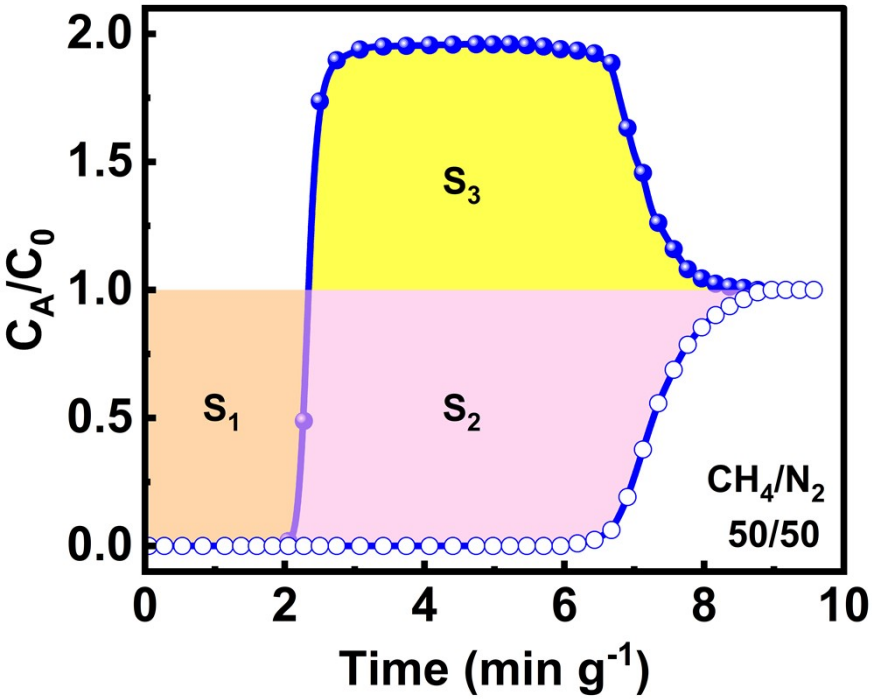

Figure S59. The calculation diagram of kinetic adsorption capacity of CH_4 or N_2.

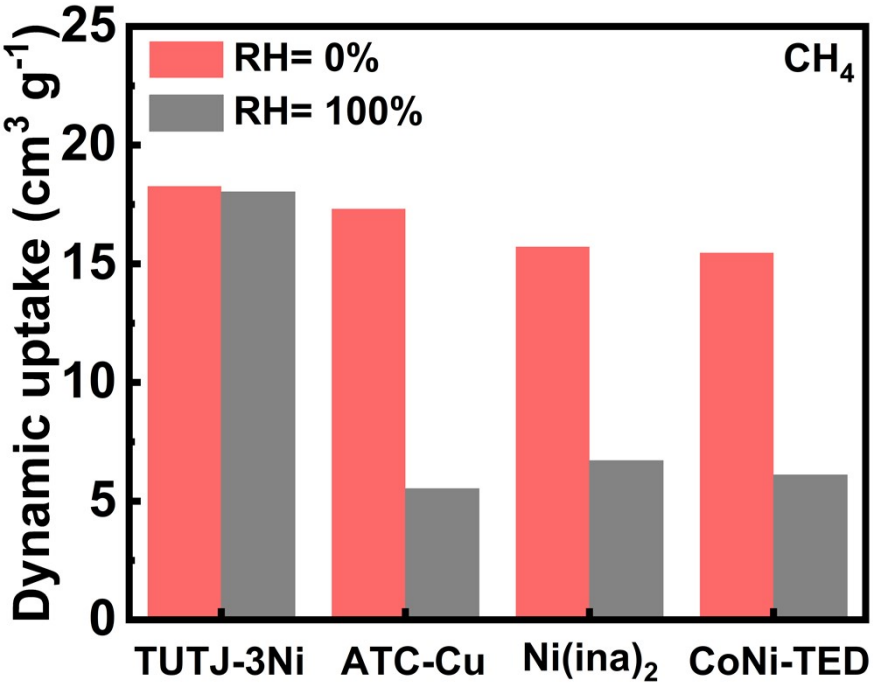

Figure S60. Comparison of dynamic CH_4 uptakes under dry and humid conditions.

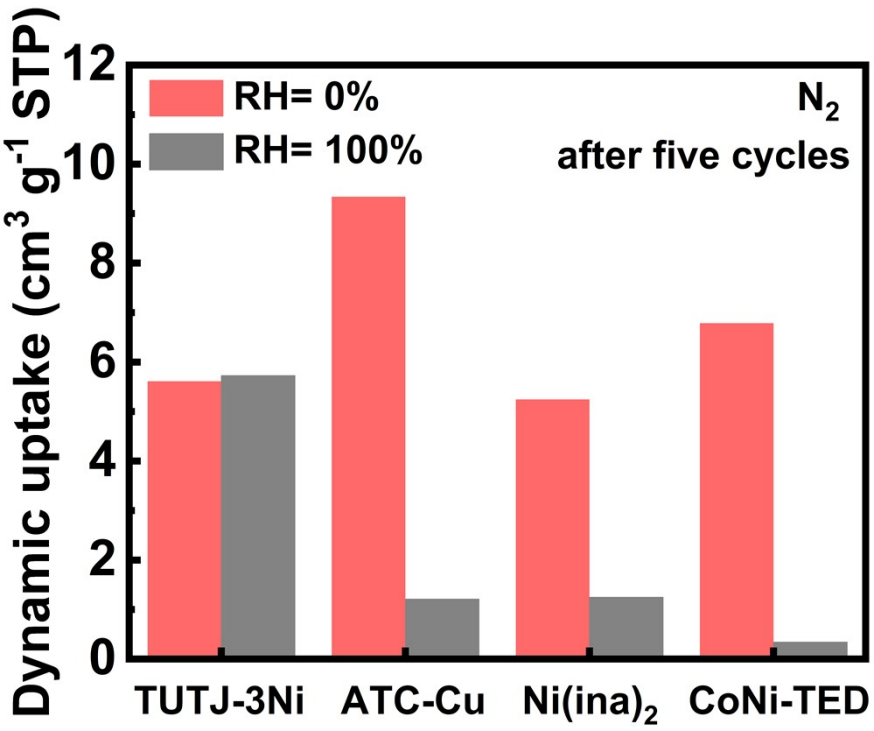

Figure S61. Comparison of dynamic N_2 uptakes under dry and humid conditions.

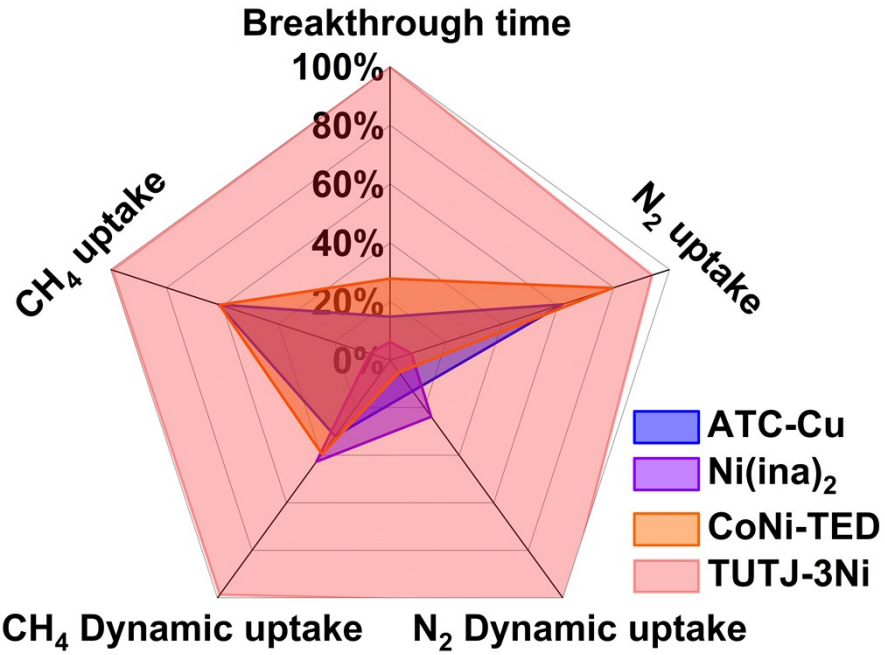

Figure S62. Radar chart showing retention (%) of breakthrough time, adsorption capacity, and dynamic uptake for four materials under 100% RH. Retention = (humid value)/(dry baseline) × 100%. Dry baseline sources: adsorption capacity – Figs. S48–S51 (dry isotherms); breakthrough time – Fig. S53 (dry breakthrough); dynamic uptake – Figs. S60–S61 (dry bars). Humid value sources: adsorption capacity – Figs. S48–S51 (humid isotherms); breakthrough time – Fig. S58 (fifth humid cycle); dynamic uptake – Figs. S60–S61 (humid bars).

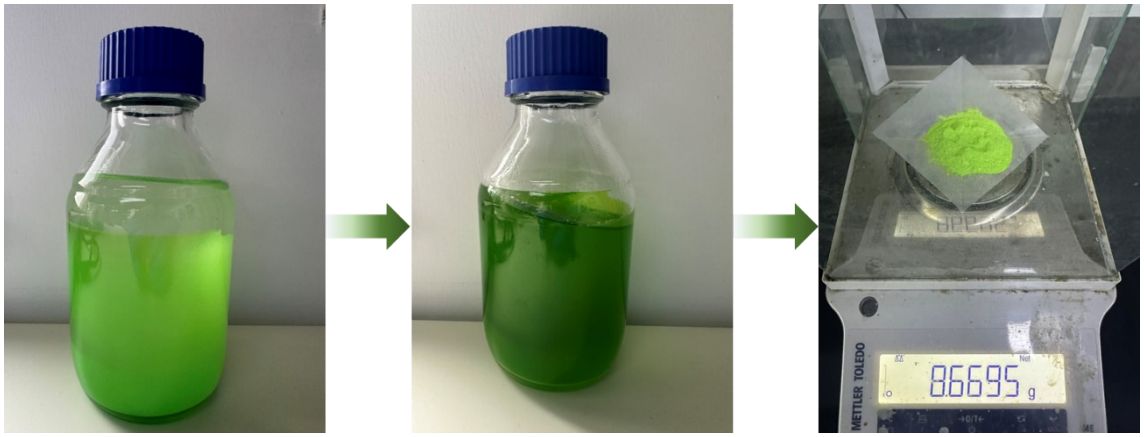

Figure S63. Scaled-up synthesis of TUTJ-3Ni via a solvothermal method.

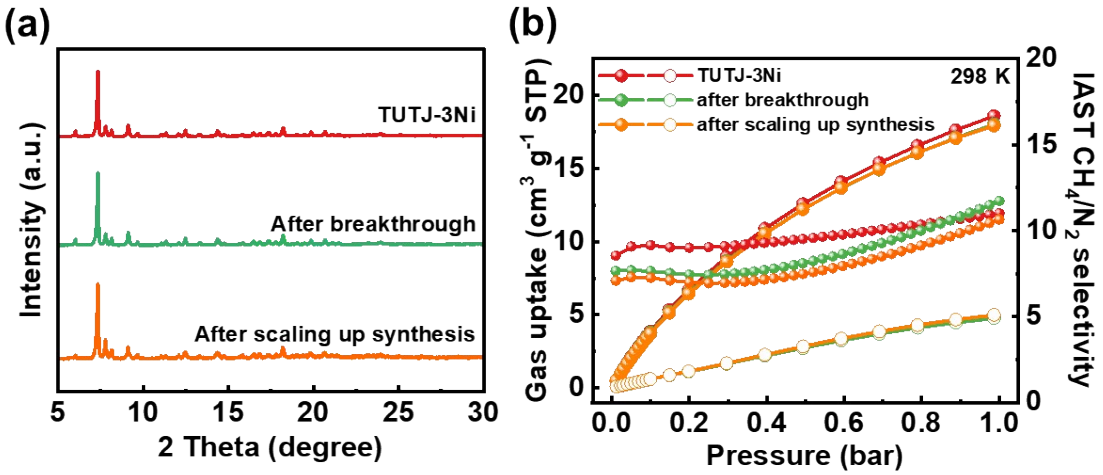

Figure S64. (a) PXRD patterns of the post-breakthrough sample and a 100× magnification TUTJ-3Ni. (b) CH_4 and N_2 sorption isotherms at 298 K for the post-breakthrough sample and a 100× magnification TUTJ-3Ni, and the corresponding IAST selectivity profile.

Table S4 Comparison of the adsorptive separation performance between TUTJ-3Ni and other reported hydrophobic adsorbents.

Adsorbent	CH_4/N_2 selectivity	Uptake ($cm^3\ g^{-1}$)		Q_{st} ($kJ\ mol^{-1}$)		ΔQ_{st} ($kJ\ mol^{-1}$)	Ref.
		CH_4	N_2	CH_4	N_2		
TUTJ-3Ni	**11.1**	**18.6**	**4.9**	**30.3**	**19.5**	**10.8**	**This work**
TUTJ-2Ni	6.2	10.5	3.0	24.0	15.0	9	
TUTQ-1Ni	11.0	19.2	4.4	22.9	18.0	4.9	[8]
NKMOF-8-Me	9.0	39.5	7.0	28.0	18.9	9.1	[9]
Al-FUM-Me	8.6	27.2	5.6	24.1	17.4	6.7	[10]
DMOF-A2	7.2	37.0	8.8	22.5	N.R.	N.R.	[11]
TUT-100	6.3	27.5	5.0	23.7	19.6	4.1	[12]
MIL-120Al	6.0	33.7	10.5	20.8	17.8	3.0	[2]
CALF-20	3.6	24.8	8.9	25.0	23.0	2.0	[13]

N.R. represents not reported.

Table S5 Comparison of the adsorptive separation performance between TUTJ-3Ni and other reported porous adsorbents.

Adsorbent	Q_{st} (kJ mol^{-1})		ΔQ_{st} (kJ mol^{-1})	CH_4/N_2 selectivity	Uptake (cm^3 g^{-1})		Ref.
	CH_4	N_2			CH_4	N_2	
TUTJ-3Ni	**30.3**	**19.5**	**10.8**	**11.1**	**18.6**	**4.9**	**This work**
$Ni(ina)_2$	28	17.9	10.1	15.8	40.8	11.9	[14]
NKMOF-8-Me	28	18.9	9.1	9	39.4	6.9	[15]
CoNi-TED	27.7	22.8	4.9	23.5	26	3	[16]
Al-CDC	27.5	18.6	8.9	13.1	32.1	5.1	[17]
ATC-Cu	26.8	16	10.8	9.7	65	16.8	[18]
$Ni(OAc)_2L$	26.7	20	6.7	7	25.8	10.5	[19]
MOF-888	26	22	4	8.4	10.1	1.8	[20]
CoNi(pyz-NH_2)	25.5	18.9	6.6	11.9	20.3	3	[21]
$Co_3(C_4O_4)_2(OH)_2$	25.1	18.1	7	12.5	9	4.1	[22]
CALF-20	25	23	2	3.6	24.8	8.9	[13]
HTD-Cu-MOF-SCH_3	24.6	17.9	6.7	15	16.4	2.2	[23]
TUTJ-201Ni	24.5	20.2	4.5	7.2	19.7	5	[24]
Al-FUM-Me	24.1	17.4	6.7	8.6	27.2	5.6	[10]
TUTJ-2Ni	**24**	**15**	**9**	**6.2**	**10.5**	**3**	**This work**
Cu(hfipbb)(H_2hfipbb)$_{0.5}$	24	20	4	6.9	10.5	2.9	[25]
ZIF-94	23.9	20	3.9	7.4	33.8	8.2	[26]
TUT-100	23.7	19.6	4.1	6.3	27.5	5	[12]
Ni-MA-BPY	23.5	19.6	3.9	7.4	22.6	4.7	[27]
SBMOF-1	23.2	16.1	7.1	11.5	20.7	4	[28]
MOF-890	23	19	4	7	24	6	[20]
TUTQ-1Ni	22.9	18	4.9	11	19.2	4.4	[8]
Co-MA-BPY	22.8	18.4	4.4	7.2	20.6	4.4	[27]
DMOF-A_2	22.5	N.R.	N.R.	7.2	37	8.8	[11]
Ni-FA	22.2	18	4.2	6	17.9	3.9	[29]
MOF-891	22	21	1	7.8	30	6.4	[20]
MOF-889	22	19	3	6.4	26	5.3	[20]
MIL-120Al	20.8	17.8	3	6	33.7	10.5	[2]
STAM-1	20	15	5	11.1	14.2	2.4	[30]
$Cu(OTf)_2$	19.6	16	3.6	4.8	5.7	1.6	[31]
Ni-Qc-5-Dia	19.5	14	5.5	7.4	29.3	6.2	[32]
[Cu(Me-4py-trz-ia)]	18	12	6	4.2	25.1	N.R.	[33]
ZIF-93	15.8	12.5	3.3	3.6	11.7	3.6	[26]
MIL-101(Cr) (293 K)	15.7	12	3.7	2.7	14.6	2.9	[34]

N.R. represents not reported.

References

1. H. Sun, COMPASS: An ab Initio Force-Field Optimized for Condensed-Phase Applications-Overview with Details on Alkane and Benzene Compounds, *Journal of Physical Chemistry B*, 1998, **102**, 7338-7364.
2. F. Zhang, H. Shang, B. Zhai, X. Li, Y. Zhang, X. Wang, J. Li and J. Yang, Thermodynamic-kinetic synergistic separation of CH_4/N_2 on a robust aluminum-based metal-organic framework, *AIChE Journal*, 2023, **69**, e18079.
3. H. Moradi, H. Azizpour, H. Bahmanyar and M. Emamian, Molecular dynamic simulation of carbon dioxide, methane, and nitrogen adsorption on Faujasite zeolite, *Chinese Journal of Chemical Engineering*, 2022, **43**, 70-76.
4. S. J. Clark, M. D. Segall, C. J. Pickard, P. J. Hasnip, M. I. J. Probert, K. Refson and M. C. Payne, First principles methods using CASTEP, *Zeitschrift für Kristallographie - Crystalline Materials*, 2005, **220**, 567-570.
5. M. J. Frisch, G. W. Trucks, H. B. Schlegel, G. E. Scuseria, M. A. Robb, J. R. Cheeseman, G. Scalmani, V. Barone, G. A. Petersson, H. Nakatsuji, X. Li, M. Caricato, A. V. Marenich, J. Bloino, B. G. Janesko, R. Gomperts, B. Mennucci, H. P. Hratchian, J. V. Ortiz, A. F. Izmaylov, J. L. Sonnenberg, Williams, F. Ding, F. Lipparini, F. Egidi, J. Goings, B. Peng, A. Petrone, T. Henderson, D. Ranasinghe, V. G. Zakrzewski, J. Gao, N. Rega, G. Zheng, W. Liang, M. Hada, M. Ehara, K. Toyota, R. Fukuda, J. Hasegawa, M. Ishida, T. Nakajima, Y. Honda, O. Kitao, H. Nakai, T. Vreven, K. Throssell, J. A. Montgomery Jr., J. E. Peralta, F. Ogliaro, M. J. Bearpark, J. J. Heyd, E. N. Brothers, K. N. Kudin, V. N. Staroverov, T. A. Keith, R. Kobayashi, J. Normand, K. Raghavachari, A. P. Rendell, J. C. Burant, S. S. Iyengar, J. Tomasi, M. Cossi, J. M. Millam, M. Klene, C. Adamo, R. Cammi, J. W. Ochterski, R. L. Martin, K. Morokuma, O. Farkas, J. B. Foresman and D. J. Fox, Gaussian 09 Revision D.01, *Gaussian, Inc., Wallingford, CT*, 2013.
6. T. Lu and F. Chen, Multiwfn: A multifunctional wavefunction analyzer, *Journal of Computational Chemistry*, 2012, **33**, 580-592.
7. W. Humphrey, A. Dalke and K. Schulten, VMD: Visual molecular dynamics, *Journal of Molecular Graphics*, 1996, **14**, 33-38.
8. Z. Zhao, Y. Li, Y. Wang, Y. Wang, Y. Tang, M. Lu, X. Yang, X. Wang, F. Zhang, J. Li and J. Yang, Hydrophobic metal-organic framework Featuring multiple O/S active sites for efficient CH_4/N_2 separation under humid conditions, *Separation and Purification Technology*, 2025, **361**, 131382.
9. M. Chang, F. Wang, Y. Wei, Q. Yang, J.-X. Wang, D. Liu and J.-F. Chen, Separation of CH_4/N_2 by an ultra-stable metal–organic framework with the highest breakthrough selectivity, *AIChE J.*, 2022, **68**, e17794.
10. M. Chang, T. Yan, Y. Wei, J.-X. Wang, D. Liu and J.-F. Chen, Enhancing CH_4 Capture from Coalbed Methane through Tuning van der Waals Affinity within Isoreticular Al-Based Metal–Organic Frameworks, *ACS Applied Materials & Interfaces*, 2022, **14**, 25374-25384.
11. T. Li, X. Jia, H. Chen, Z. Chang, L. Li, Y. Wang and J. Li, Tuning the Pore Environment of MOFs toward Efficient CH_4/N_2 Separation under Humid Conditions, *ACS Applied Materials & Interfaces*, 2022, **14**, 15830-15839.
12. J. Liu, X. Tang, X. Liang, L. Wu, F. Zhang, Q. Shi, J. Yang, J. Dong and J. Li, Superhydrophobic zeolitic imidazolate framework with suitable SOD cage for effective CH_4/N_2 adsorptive separation in humid environments, *AIChE J.*, 2022, **68**, e17589.
13. J. Su, J. Li, J. Xu, Y. Li, R. Zhang, D. Lv, F. Xu, J. Peng, X. Wang, J. Yan, Z. Liu, X. Chen, H. Xi and Q. Xia, Cost-Effective Zinc-Based Metal–Organic Framework for Highly Efficient Methane Purification, *Industrial & Engineering Chemistry Research*, 2024, **63**, 18544-18551.
14. S.-M. Wang, M. Shivanna and Q.-Y. Yang, Nickel-based metal–organic frameworks for coal-bed methane purification with Record CH_4/N_2 selectivity, *Angew. Chem. Int. Ed.*, 2022, **61**, e202201017.
15. M. Chang, F. Wang, Y. Wei, Q. Yang, J.-X. Wang, D. Liu and J.-F. Chen, Separation of CH_4/N_2 by an ultra-stable metal–organic framework with the highest breakthrough selectivity, *AIChE J.*, 2022, **68**, e17794.
16. P. Guo, J. Fu, B. Xue, T. Wang, L. Yang, Y. Ying, Q. Yang and D. Liu, One Flexible Metal–Organic Framework with Guest-Adaptive Rotational Valve for Gas Separation, *Advanced Functional Materials*, 2025, **35**, 2500210.
17. M. Chang, Y. Zhao, D. Liu, J. Yang, J. Li and C. Zhong, Methane-trapping metal–organic frameworks with an aliphatic ligand for efficient CH_4/N_2 separation, *Sustainable Energy Fuels.*, 2020, **4**, 138-142.
18. Z. Niu, X. Cui, T. Pham, P. C. Lan, H. Xing, K. A. Forrest, L. Wojtas, B. Space and S. Ma, A metal–organic framework based methane nano-trap for the capture of coal-mine methane, *Angew. Chem. Int. Ed.*, 2019, **58**, 10138-10141.
19. C. E. Kivi, B. S. Gelfand, H. Dureckova, H. T. K. Ho, C. Ma, G. K. H. Shimizu, T. K. Woo and D. Song, 3D porous metal–organic framework for selective adsorption of methane over dinitrogen under ambient pressure, *Chemical Communications*, 2018, **54**, 14104-14107.
20. P. T. K. Nguyen, H. T. D. Nguyen, H. Q. Pham, J. Kim, K. E. Cordova and H. Furukawa, Synthesis and selective CO_2 capture properties of a series of hexatopic linker-based metal–organic frameworks, *Inorg. Chem.*, 2015, **54**, 10065-10072.
21. P. Guo, Y. Ying and D. Liu, One Scalable and Stable Metal–Organic Framework for Efficient Separation of CH_4/N_2 Mixture, *ACS Applied Materials & Interfaces*, 2024, **16**, 7338-7344.
22. L. Li, L. Yang, J. Wang, Z. Zhang, Q. Yang, Y. Yang, Q. Ren and Z. Bao, Highly efficient separation of methane from nitrogen on a squarate-based metal-organic framework, *AIChE J.*, 2018, **64**, 3681-3689.
23. M. Chang, J. Ren, Y. Wei, T. Yan, J.-X. Wang, D. Liu and J.-F. Chen, Discovery of a Scalable Metal–Organic Framework with a Switchable Structure for Efficient CH_4/N_2 Separation, *Chemistry of Materials*, 2023, **35**, 4286-4296.
24. F. Zhang, Y. Tang, Z. Zhao, M. Lu, X. Wang, J. Li and J. Yang, Construction of a novel nickel-based MOF with accessible oxygen sites for efficient CH_4/N_2 separation, *Inorganic Chemistry Frontiers*, 2024, **11**, 3889-3896.
25. X. Wu, B. Yuan, Z. Bao and S. Deng, Adsorption of carbon dioxide, methane and nitrogen on an ultramicroporous copper metal–organic framework, *J. Colloid Interface Sci.*, 2014, **430**, 78-84.

26. Q. Shi, J. Wang, H. Shang, H. Bai, Y. Zhao, J. Yang, J. Dong and J. Li, Effective CH_4 enrichment from N_2 by SIM-1 via a strong adsorption potential SOD cage, *Sep. Purif. Technol.*, 2020, **230**, 115850.
27. X.-W. Liu, Y.-M. Gu, T.-J. Sun, Y. Guo, X.-L. Wei, S.-S. Zhao and S.-D. Wang, Water resistant and flexible MOF materials for highly efficient separation of methane from nitrogen, *Ind. Eng. Chem. Res.*, 2019, **58**, 20392-20400.
28. M. Chang, J. Ren, Q. Yang and D. Liu, A robust calcium-based microporous metal-organic framework for efficient CH_4/N_2 separation, *Chem. Eng. J.*, 2021, **408**, 127294.
29. X.-W. Liu, Y. Guo, A. Tao, M. Fischer, T.-J. Sun, P. Z. Moghadam, D. Fairen-Jimenez and S.-D. Wang, "Explosive" synthesis of metal-formate frameworks for methane capture: an experimental and computational study, *Chemical Communications*, 2017, **53**, 11437-11440.
30. M. Chang, Y. Zhao, Q. Yang and D. Liu, Microporous Metal–Organic Frameworks with Hydrophilic and Hydrophobic Pores for Efficient Separation of CH_4/N_2 Mixture, *ACS Omega*, 2019, **4**, 14511-14516.
31. X. Wang, L. Li, J. Yang and J. Li, CO_2/CH_4 and CH_4/N_2 separation on isomeric metal organic frameworks, *Chin. J. Chem. Eng.*, 2016, **24**, 1687-1694.
32. S. Qadir, Y. Gu, S. Ali, D. Li, S. Zhao, S. Wang, H. Xu and S. Wang, A thermally stable isoquinoline based ultra-microporous metal-organic framework for CH_4 separation from coal mine methane, *Chem. Eng. J.*, 2022, **428**, 131136.
33. J. Möllmer, M. Lange, A. Möller, C. Patzschke, K. Stein, D. Lässig, J. Lincke, R. Gläser, H. Krautscheid and R. Staudt, Pure and mixed gas adsorption of CH_4 and N_2 on the metal–organic framework Basolite® A100 and a novel copper-based 1,2,4-triazolyl isophthalate MOF, *J. Mater. Chem.*, 2012, **22**, 10274-10286.
34. J. Pérez-Pellitero, H. Amrouche, F. R. Siperstein, G. Pirngruber, C. Nieto-Draghi, G. Chaplais, A. Simon-Masseron, D. Bazer-Bachi, D. Peralta and N. J. C. A. E. J. Bats, Adsorption of CO_2, CH_4, and N_2 on zeolitic imidazolate frameworks: experiments and simulations, *Chem. Eur. J.*, 2010, **16**, 1560-1571.